Limiting masses and radii of neutron stars and their implications

Christian Drischler,[1,2,*] Sophia Han,[1,3,†] James M. Lattimer,[4,‡] Madappa Prakash,[3,§] Sanjay Reddy,[5,¶] and Tianqi Zhao[4,**]

[1] *Department of Physics, University of California, Berkeley, CA 94720, USA*
[2] *Nuclear Science Division, Lawrence Berkeley National Laboratory, Berkeley, CA 94720, USA*
[3] *Department of Physics and Astronomy, Ohio University, Athens, OH 45701, USA*
[4] *Department of Physics and Astronomy, Stony Brook University, Stony Brook, NY 11794, USA*
[5] *Institute for Nuclear Theory, University of Washington, Seattle, WA 98195, USA*

(Dated: September 12, 2020)

We combine equation of state of dense matter up to twice nuclear saturation density ($n_{\rm sat} = 0.16\,{\rm fm}^{-3}$) obtained using chiral effective field theory (χEFT), and recent observations of neutron stars to gain insights about the high-density matter encountered in their cores. A key element in our study is the recent Bayesian analysis of correlated EFT truncation errors based on order-by-order calculations up to next-to-next-to-next-to-leading order in the χEFT expansion. We refine the bounds on the maximum mass imposed by causality at high densities, and provide stringent limits on the maximum and minimum radii of $\sim 1.4\,{\rm M}_\odot$ and $\sim 2.0\,{\rm M}_\odot$ stars. Including χEFT predictions from $n_{\rm sat}$ to $2\,n_{\rm sat}$ reduces the permitted ranges of the radius of a $1.4\,{\rm M}_\odot$ star, $R_{1.4}$, by $\sim 3.5\,{\rm km}$. If observations indicate $R_{1.4} < 11.2\,{\rm km}$, our study implies that either the squared speed of sound $c_s^2 > 1/2$ for densities above $2\,n_{\rm sat}$, or that χEFT breaks down below $2\,n_{\rm sat}$. We also comment on the nature of the secondary compact object in GW190814 with mass $\simeq 2.6\,{\rm M}_\odot$, and discuss the implications of massive neutron stars $> 2.1\,{\rm M}_\odot$ $(2.6\,{\rm M}_\odot)$ in future radio and gravitational-wave searches. Some form of strongly interacting matter with $c_s^2 > 0.35\,(0.55)$ must be realized in the cores of such massive neutron stars. In the absence of phase transitions below $2\,n_{\rm sat}$, the small tidal deformability inferred from GW170817 lends support for the relatively small pressure predicted by χEFT for the baryon density $n_{\rm B}$ in the range $1-2\,n_{\rm sat}$. Together they imply that the rapid stiffening required to support a high maximum mass should occur only when $n_{\rm B} \gtrsim 1.5 - 1.8\,n_{\rm sat}$.

I. INTRODUCTION

The maximum mass, $M_{\rm max}$, and radii of neutron stars (NSs) are related to each other by the equation of state (EOS) of dense matter and both can be accessed by observations. Primary constraints on $M_{\rm max}$ come from observations and have a number of astronomical and physical implications. $M_{\rm max}$ is predominately determined by the EOS at densities higher than three times nuclear saturation density, $n_{\rm sat} \simeq 0.16\,{\rm fm}^{-3}$ [1], and is therefore a probe of the nature of high-density matter. Pinning down $M_{\rm max}$ enables the exploration of the phases of cold and dense matter in the strongly coupled region of quantum chromodynamics (QCD) as well as the determination of the pressure vs energy density relation (or the EOS) of such phases. The radii of canonical NSs with masses $\simeq 1.4\ {\rm M}_\odot$, on the other hand, are largely determined by the EOS at densities less than $3\,n_{\rm sat}$ [2].

$M_{\rm max}$ also fixes the minimum mass of a stellar mass $\mathcal{O}({\rm M}_\odot)$ black hole (BH). It is therefore a crucial factor in determining the final fate of core-collapse supernovae and binary neutron star (BNS) mergers. In core-collapse supernovae, the formation of a BH will depend on the amount of fall-back matter and will be sensitive to the nature of the progenitor and neutrino emission after the initial formation of a proto-neutron star. In BNS mergers, the formation of a BH depends on the total inspiralling mass, mass ejection, and the extent of rotational and magnetohydrodynamic support [3, 4]. Now that at least a few mergers involving NS have been detected through gravitational-wave (GW) radiation, and many more are anticipated in the near future, improved constraints on $M_{\rm max}$ will become available. As the high-frequency capabilities of GW detectors are improved, the detection of post-merger radiation will profoundly influence our knowledge of $M_{\rm max}$. Already, knowledge of $M_{\rm max}$ would determine the nature of the components of the recently observed mergers GW190425 and GW190814, both of which show indications of having a component with a mass larger than $2\,{\rm M}_\odot$ that either could be a heavy NS or a light BH. If concomitant electromagnetic (EM) signals are also detected from future GW events, as they were in the BNS merger GW170817 [5–7], additional information about $M_{\rm max}$ becomes available [3, 4].

On the theoretical front, $M_{\rm max}$ plays a crucial role in determining both the minimum and maximum radius as a function of the NS mass M. Therefore, besides the important contributions from radio and X-ray binary pulsar observations that have accurately measured several NS masses and provided a lower bound $M_{\rm max} \gtrsim 2\,{\rm M}_\odot$ [8–12], GW and X-ray data that can simultaneously determine NS masses and radii offer important constraints. So far, the radii inferred from X-ray observa-

* cdrischler@berkeley.edu
† sjhan@berkeley.edu
‡ james.lattimer@stonybrook.edu
§ prakash@ohio.edu
¶ sareddy@uw.edu
** tianqi.zhao@stonybrook.edu

tions (see Ref. [13] for a review) of quiescent low-mass X-ray binaries (QLMXBs) [14], photospheric radius expansion bursts (PREs) [15], and pulse-profiles from rotation-powered millisecond pulsars [16], together with the first GW detection of the BNS merger GW170817 [5, 6], have mostly been of NSs with canonical masses around $1.4\,\mathrm{M}_\odot$. Consequently, the *Neutron Star Interior Composition ExploreR* (NICER) proposal [17] to measure the radii of relatively massive NSs such as PSR J1614-2230 ($M \simeq 1.91\,\mathrm{M}_\odot$ [8, 10, 11]) and PSR J0740+6620 ($M \simeq 2.14\,\mathrm{M}_\odot$ [12]) is of considerable interest. The same is true of future radio observations using the *Square Kilometre Array* (SKA) telescope [18], etc. from binary pulsars that could reveal even more massive NSs.

The purpose of this paper is to explore the interplay between $M_{\rm max}$ and NS radii and to confront theoretical expectations with currently available observational constraints. An earlier study [2] showed that the radii of $\simeq 1.4\,\mathrm{M}_\odot$ NSs are strongly correlated with the pressure of matter in the density range $1-3\,n_{\rm sat}$. In the important density range $\lesssim 2\,n_{\rm sat}$, chiral effective field theory (χEFT) with pion and nucleon degrees of freedom has become the dominant microscopic approach to describing nuclear interactions [19–22]. Applying χEFT to the EOS of infinite nuclear matter and the structure of neutron stars [23–37] has enabled significant progress (see also Refs. [38–40] for recent reviews). A notable development is the quantification of theoretical uncertainties in a statistically robust way. Recently, the BUQEYE collaboration [41] has introduced a novel framework for quantifying correlated EFT truncation errors in infinite-matter calculations. In a first application, they have conducted a statistical analysis of the zero-temperature EOS with χEFT nucleon-nucleon (NN) and three-nucleon (3N) interactions up to next-to-next-to-next-to-leading order (N^{3}LO) [42, 43] using Gaussian Processes (GPs). This study was motivated by recent advances in many-body perturbation theory (MBPT) [35] that have enabled improved χEFT predictions of the pure neutron matter (PNM) EOS at this order, and, for the first time, order-by-order calculations in symmetric nuclear matter (SNM) based on χEFT NN and 3N forces up to N^{3}LO [35, 42, 44].

In this paper, we use BUQEYE's analysis of the EOS in the limits of PNM and SNM up to $2\,n_{\rm sat}$ to construct the EOS of charge neutral and beta-stable neutron-star matter (NSM). This is coupled to a standard NS crust for densities $\lesssim 0.5\,n_{\rm sat}$ and extrapolations for densities $\gtrsim 2.0\,n_{\rm sat}$ to assess the overall impact on NS structure. One goal of this study is to address quantitatively the extent to which EOS knowledge at $\sim 2.0\,n_{\rm sat}$ can inform us about the NS maximum mass, and how it can be combined with observations of massive NSs to constrain the properties of matter encountered at the highest densities in their cores. Another goal is to derive model-independent bounds on the radii of NSs with masses in the range $1-2\,\mathrm{M}_\odot$.

As the squared speed of sound c_s^2 reflects the stiffness of the EOS, we probe both maximum and minimum radius bounds by matching the N^{3}LO results, including possible extrapolations up to $3.0\,n_{\rm sat}$, with a constant sound speed beyond a matching density $n_{\rm m}$. The existence of nuclei, observations of accreting NSs that implicate the presence of neutron-rich nuclei in the NS crust, and heavy ion collisions (HICs) at intermediate energies together provide compelling circumstantial evidence to indicate that $n_{\rm m} > n_{\rm sat}$, and in this work we consider $1.0 \le n_{\rm m}/n_{\rm sat} \le 3.0$. The use of the maximally stiff EOS with $c_s^2 = 1$ (the causal limit) for $n_{\rm B} > n_{\rm m}$ establishes firm upper bounds both on $M_{\rm max}$ and the radius as a function of mass. In addition, we also consider energy density discontinuities at $n_{\rm m}$ to refine minimum bounds on radii as functions of mass for specified values of $M_{\rm max}$. We also explore models with smaller c_s^2 at high density to ascertain maximum possible sound speeds from values of $M_{\rm max}$ and mass-radius (M–R) observations.

The discovery of a massive secondary compact object with mass $\sim 2.6\,\mathrm{M}_\odot$ through GW observations of the binary merger GW190814 generated a flurry of articles addressing if this object can be a NS, and, if so, its possible implications [45–52]. Our results complement earlier studies, but go beyond in several aspects. Most significantly,

(i) we consistently include statistically meaningful EFT truncation errors in the EOS of NSM up to N^{3}LO, and determine its range of applicability, to provide a framework for constraining $M_{\rm max}$ and NS radii,

(ii) we identify correlations of NS radii and tidal deformabilities with $M_{\rm max}$, together with their possible implications for the EOS at densities $\gtrsim 2.0\,n_{\rm sat}$, and

(iii) we show how these correlations and future observations can tighten current bounds on NS masses and radii.

This paper is organized as follows. In Sec. II we discuss the bounds imposed by causality and the scaling relations for the masses and radii of NSs. Section III contains details of the various EOSs used along with the rationale for their choice. Our results and their discussion in light of the current observational constraints and possible future findings are presented in Sec. IV. An overall discussion and comparison with pertinent recent works are contained in Sec. V. Our concluding remarks are given in Sec. VI. We use natural units in which $\hbar = c = 1$ unless explicitly specified.

II. BOUNDS IMPOSED BY CAUSALITY

The assumption of causality, i.e., that the maximum sound speed $c_s = \sqrt{dP/d\varepsilon}$ is unity in units of c, can establish relations limiting both minimum and maximum

radii, as functions of mass, for NS. These limits will explicitly depend on assumptions concerning the NS maximum mass $M_{\rm max}$. These causal bounds can be improved with the consideration of nuclear physics inputs as will be discussed in Sec. IV. The causality limit is imposed by using the EOS

$$P(\varepsilon) = P_0 + (\varepsilon - \varepsilon_0) \tag{1}$$

for the pressure $P > P_0$ and the energy density $\varepsilon > \varepsilon_0$.

The minimum radius as a function of mass $R_{\rm min}(M)$ for any EOS is conjectured [53] to result from using Eq. (1) with $P_0 = 0$, $P = 0$ for $\varepsilon \le \varepsilon_0$ (i.e., a self-bound star). In this case, the EOS has a single parameter (ε_0) and solutions of the Tolman-Oppenheimer–Volkoff (TOV) equation [54, 55] scale with it. Letting m be the mass enclosed within the radius r, one can define

$$r = x\frac{c^2}{\sqrt{G\varepsilon_0}}, \quad m = y\frac{c^4}{\sqrt{G^3\varepsilon_0}}, \quad \text{and} \quad P = z\varepsilon_0, \tag{2}$$

where $y(x)$ and $z(x)$ are dimensionless functions, with the boundary conditions $y_c = y(x=0) = 0$ and $z_c = z(x = 0) > 0$ at the stellar center, and $y_s = y(x = x_s)$ and $z(x = x_s) = 0$ at the stellar surface x_s. The quantities y_s and x_s depend on z_c. For small x_s, $y_s \propto x_s^3$, as expected. It should also be noted that the EOS Eq. (1) implies that the baryon number density is

$$n_{\rm B} = n_0\sqrt{\frac{\varepsilon + P}{\varepsilon_0 + P_0}}, \tag{3}$$

with $n_0 = (\varepsilon_0 + P_0)/\mu_0$ and μ_0 being the baryon chemical potential at ε_0.

In the case that $P_0 = 0$, the central baryon density is $n_{\rm cent} = n_0\sqrt{1+2z_c}$. Also, the maximum mass configuration occurs for $dy_s/dx_s = 0$, or when $x_{\rm max,s} = 0.2405$, $y_{\rm max,s} = 0.08513$, and $z_{\rm max,c} = 2.023$ (and therefore $n_{\rm max,c}/n_0 = 2.246$). The maximum mass can then be expressed as

$$M_{\rm max} = \frac{y_{\rm max,s}c^4}{\sqrt{G^3\varepsilon_0}} \simeq 4.09\sqrt{\frac{\varepsilon_{\rm sat}}{\varepsilon_0}}\,{\rm M}_\odot, \tag{4}$$

and the radius of the maximum mass configuration is

$$R_{M_{\rm max}} = \frac{x_{\rm max,s}c^2}{\sqrt{G\varepsilon_0}} \simeq 17.1\sqrt{\frac{\varepsilon_{\rm sat}}{\varepsilon_0}}\ {\rm km}. \tag{5}$$

The central energy density for the maximum mass configuration is $\varepsilon_{\rm max,c} = (z_{\rm max,c} + 1)\,\varepsilon_0$, or using Eq. (4) to eliminate ε_0,

$$\varepsilon_{\rm max,c} \simeq 50.8\left(\frac{{\rm M}_\odot}{M_{\rm max}}\right)^2\varepsilon_{\rm sat}, \tag{6}$$

where $\varepsilon_{\rm sat} \simeq 150\,{\rm MeV\,fm^{-3}}$ is the energy density at $n_{\rm sat}$. This must be the largest energy density found in any NS and it scales with $M_{\rm max}^{-2}$. The maximum baryon density is

$$n_{\rm max,c} \simeq 37.6\frac{m_{\rm B}}{\mu_0}\left(\frac{M_{\rm max}}{{\rm M}_\odot}\right)^2 n_{\rm sat}, \tag{7}$$

where $\mu_0 \sim m_{\rm B}$, the baryon mass. As an example, if one assumes that $M_{\rm max} = 2.6\,{\rm M}_\odot$ and $\mu_0 = m_{\rm B}$, it is found that $\varepsilon_0 = 2.475\,\varepsilon_{\rm sat}$, $\varepsilon_{\rm max,c} = 7.48\,\varepsilon_{\rm sat}$ and $n_{\rm max,c} = 5.56\,n_{\rm sat}$.

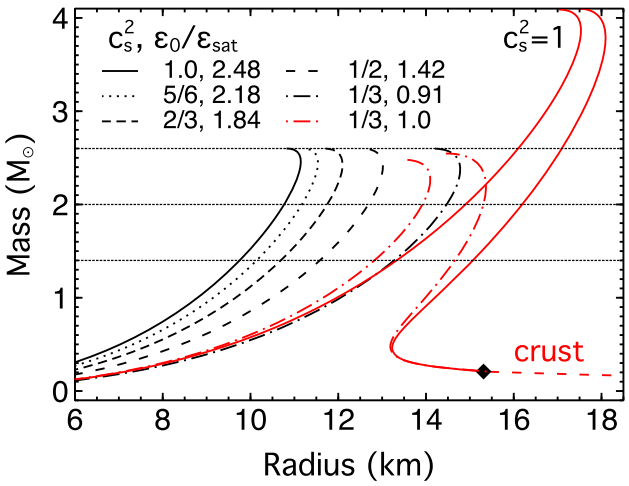

FIG. 1. The mass as a function of radius for the EOS Eq. (9) with $P_0 = 0$, $P = 0$ for $\varepsilon < \varepsilon_0$, and various values for c_s^2 with fixed $M_{\rm max} = 2.6\,{\rm M}_\odot$, are shown as five black curves (see legend). These curves correspond to the minimum possible radius $R_{\rm min}(M)$, for different maximum values of the sound speed. The four red curves correspond to $\varepsilon_0 = \varepsilon_{\rm sat}$, either $c_s^2 = 1$ (and $M_{\rm max} \simeq 4.09\,{\rm M}_\odot$) or $c_s^2 = 1/3$ (and $M_{\rm max} \simeq 2.48\,{\rm M}_\odot$) for $P > P_0$, and either $P_0 = 0$ (self-bound) or $P_0 = 0.02\,\varepsilon_0 \simeq 3\,{\rm MeV\,fm^{-3}}$ and a normal crust EOS for $P < P_0$ (maximum possible radii $R_{\rm max}(M)$); the configuration where $\varepsilon_c = \varepsilon_{\rm sat}$ is indicated by a diamond.

The dimensionless M–R curve for the causal self-bound configuration is thus defined by $y_s(x_s)$. Its *dimensionful* radius, as a function of mass, is conjectured to be the minimum radius for any configuration, $R_{\rm min}(M)$. It scales with ε_0 and therefore with the assumed value of the maximum mass:

$$R_{\rm min} = \frac{GM_{\rm max}x_s}{y_{\rm max,s}c^2} = \frac{GM_{\rm max}}{y_{\rm max,s}c^2}y_s^{-1}\left(y_{\rm max,s}\frac{M}{M_{\rm max}}\right), \tag{8}$$

and increases as $M_{\rm max}$ increases. The cases with $M_{\rm max} = 2.6\,{\rm M}_\odot$ and $M_{\rm max} = 4.09\,{\rm M}_\odot$ for which ε_0 is $2.48\,\varepsilon_{\rm sat}$ and $\varepsilon_{\rm sat}$, respectively, are shown in Fig. 1. For the case that $M_{\rm max} = 2.0\,{\rm M}_\odot$ for which $\varepsilon_0 = 4.2\,\varepsilon_{\rm sat}$, we obtain $R_{\rm min}(1.4\,{\rm M}_\odot) = 8.2\,{\rm km}$ and $R_{M_{\rm max}} = 8.4\,{\rm km}$.

TABLE I. Maximum mass solutions for the EOS Eq. (9) with $P_0 = 0$. The last two columns give the minimum radii in km for $1.4\,\mathrm{M}_\odot$ and $2.0\,\mathrm{M}_\odot$ stars, respectively, assuming $M_{\rm max} = 2.6\,\mathrm{M}_\odot$.

c_s^2	$x_{\mathrm{max},s}$	$y_{\mathrm{max},s}$	$z_{\mathrm{max,c}}$	$R_{\mathrm{min},1.4}$	$R_{\mathrm{min},2.0}$
1	0.2405	0.08513	2.023	9.75	10.8
5/6	0.2329	0.07992	1.884	10.1	11.2
2/3	0.2234	0.07328	1.705	10.7	11.7
1/2	0.2105	0.06439	1.499	11.6	12.7
1/3	0.1908	0.05169	1.277	13.3	14.5

If the assumed maximum sound speed is less than c, $R_{\rm min}(M)$ will increase. Assuming the sound speed never exceeds a given value of c_s, $R_{\rm min}(M)$ can be found using

$$P = P_0 + c_s^2(\varepsilon - \varepsilon_0), \tag{9}$$

with $P_0 = 0$ and $P = 0$ for $\varepsilon < \varepsilon_0$. Once again, the TOV equation can be rendered into dimensionless form using Eq. (2). Now, however, the baryon number density becomes

$$n_{\rm B} = n_0 \left(\frac{P+\varepsilon}{P_0+\varepsilon_0}\right)^{1/(1+c_s^2)} \tag{10}$$

and

$$n_{\rm cent} = n_0 \left[1 + z_c\left(1 + c_s^{-2}\right)\right]^{1/(1+c_s^2)}. \tag{11}$$

The dimensionless M–R curve $y_s(x_s)$ changes, as do the properties of the maximum mass configuration $x_{\mathrm{max,s}}$, $y_{\mathrm{max,s}}$ and $z_{\mathrm{max,c}}$. Figure 1 shows M–R solutions for $c_s^2 = 1, 5/6, 2/3, 1/2$, and $1/3$, all scaled so that $M_{\rm max} = 2.6\,\mathrm{M}_\odot$. In the case $c_s^2 = 1$, one finds

$$R_{\mathrm{min},1.4} = 9.75\,\mathrm{km} \quad \text{and} \quad R_{\mathrm{min},2.0} = 10.8\,\mathrm{km}\,. \tag{12}$$

Approximately, the minimum radii for smaller values of c_s scale as $c_s^{-1/2}$ [56], and for $c_s^2 = 1/3$, one finds that

$$R_{\mathrm{min},1.4} \simeq 13.3\ \mathrm{km} \quad \text{and} \quad R_{\mathrm{min},2.0} \simeq 14.5\ \mathrm{km}\,. \tag{13}$$

$\varepsilon_{\mathrm{max,c}}/\varepsilon_{\rm sat}$ is proportional to $z_{\mathrm{max,c}}+1$, which for $c_s^2 < 1$, is seen to scale roughly as $c_s^{3/2}$. Relevant properties of these solutions are given in Table I.

Stars with $P_0 = 0$ are often referred to as *self-bound* stars. In contrast, normal NSs have a low-density crust with $P_0 > 0$. For normal stars, $R_{\rm min}(M)$ will be larger than those shown in Fig. 1. Generally, the radius will increase with the assumed values of ε_0 and P_0 for a given value of c_s, and, to a lesser degree, will also depend on the crust EOS for $P < P_0$. Most importantly, since $M_{\rm max}$ and ε_0 remain closely related, $R_{\rm min}(M)$ will be very sensitive to the lower limit to $M_{\rm max}$. Details and implications are discussed in Sec. IV C.

Ironically, the maximum radius as a function of mass $R_{\rm max}(M)$ can also be found by appending the same EOS Eq. (9) at a matching density $n_{\rm m}$ or $\varepsilon_{\rm m}$ onto an assumed lower-density (crust) EOS. This is because Eq. (9) is the stiffest possible EOS for an assumed maximum value of the sound speed c_s. Although the same EOS is used, the $R_{\rm min}(M)$ bound involves a finite surface energy density $\varepsilon_0 = \varepsilon_{\rm m}$, while the $R_{\rm max}(M)$ bound is assumed to lack a discontinuity in ε when appending the crust[1]. The resulting $R_{\rm max}(M)$ trajectory, and $M_{\rm max}$, will depend on the matching density $\varepsilon_{\rm m}$ and pressure $P_{\rm m}$, the crust EOS, and assumed maximum sound speed c_s, and both roughly scale as $\varepsilon_{\rm m}^{-1/2}$. Since there is no evidence that a transition to a non-hadronic EOS occurs for densities smaller than $\varepsilon_{\rm sat}$, a limiting set of $R_{\rm max}(M)$ curves is found assuming $\varepsilon_{\rm m} = \varepsilon_{\rm sat}$. As the matching pressure $P_{\rm m}$ is not negligibly small, $P_{\rm m} \simeq 0.02\,\varepsilon_{\rm sat}$ for $\varepsilon_{\rm m} \simeq \varepsilon_{\rm sat}$, the $M-R$ curve is considerably altered, and forms a maximum radius trajectory $R_{\rm max}(M)$ which lies at a larger radius for each mass than $R_{\rm min}(M)$, as can be seen by comparing the two solid red curves for $c_s^2 = 1$ in Fig. 1. $R_{\rm max}$ for $c_s^2 = 1$ can be safely assumed to give, approximately, the largest possible radii for normal NS (it varies with the assumed EOS below $\varepsilon_{\rm m}$). It is interesting that the maximum masses with $\varepsilon_{\rm m} = \varepsilon_{\rm sat}$ for a self-bound star (left red solid curve) and for a normal star with a crust (right red solid curve) are nearly identical and are substantially larger than $2.6\,\mathrm{M}_\odot$, for example. Lower maximum masses are obtained if the matching density is increased, which decreases $R_{\rm max}(M)$ as well. An observed upper limit on $M_{\rm max}$ below $4.09\,\mathrm{M}_\odot$ will automatically alter the $R_{\rm max}$ boundary, however, because in this case either $\varepsilon_{\rm m}$ would have to increase or c_s would have to decrease to correspondingly reduce $M_{\rm max}$.

The situation is similar if a lower fixed sound speed is assumed. Figure 1 also displays $R_{\rm min}(M)$ and $R_{\rm max}(M)$ trajectories for $c_s^2 = 1/3$ for the self-bound and realistic crust cases (the left and right red dot-dashed curves, respectively), which have smaller radii and $M_{\rm max}$ values than for $c_s^2 = 1$. Note that $R_{\rm max}(M)$ for $c_s^2 = 1/3$ (right red dot-dashed curve) can become smaller than $R_{\rm min}(M)$ for $c_s^2 = 1$ and $P_0 = 0$ (left red solid curve) for $M \gtrsim 2.3\,\mathrm{M}_\odot$, suggesting that $c_s^2 = 1/3$ is incompatible with the assumption that $M_{\rm max} = 2.6\,\mathrm{M}_\odot$; the maximum value of c_s^2 must be larger than $1/3$ in the interior of a $2.6\,\mathrm{M}_\odot$ star, or $P_0 > 0$ (i.e., there is a crust), or $M_{\rm max} < 2.6\,\mathrm{M}_\odot$.

A more realistic maximum radius boundary will depend on both the matching density and the EOS below that density. In the next section we discuss realistic constraints on this portion of the EOS stemming from theoretical studies of NSM.

[1] Note that if a discontinuity in ε is assumed at $\varepsilon_{\rm m}$, a smaller $R_{\rm max}$ trajectory is obtained, but one with a correspondingly smaller $M_{\rm max}$ as well. This situation is briefly discussed in Sec. IV B.

III. CONSTRUCTION OF THE EOS

The EOS up to the core-crust boundary of NSs at $\approx 0.5\,n_{\rm sat}$ is generally considered to be well-understood [57, 58]. Because nucleons contribute $\lesssim 10\%$ to the crust pressure, uncertainties in the NN potential only weakly propagate into the crust EOS. The proton fraction in matter at densities higher than the core-crust boundary is relatively small, so that the EOS in the vicinity of the saturation density is dominated by that of PNM. The admixture of protons and leptons produce small corrections, which are effectively minimized because of the requirement that NSM be in beta equilibrium; that is, the total energy is minimized with respect to the proton fraction.

During the past few years, there have been important theoretical advances in the understanding of dense nuclear matter in the density regime $\lesssim 2.0\,n_{\rm sat}$ from χEFT studies. χEFT [19–22] exploits the *separation of scales* that arises due to the gap between the masses of the (pseudo-)Goldstone bosons of chiral symmetry breaking—the pions—and energy scales associated with interactions at shorter length scales. While the long-range pion exchanges are explicitly resolved in χEFT, short-range interactions are given by contact interactions whose low-energy couplings need to be fit to experimental data. The momentum scale associated with the interactions at short-distances is denoted by Λ_b, and is called the breakdown scale of the EFT. When the relative momentum between nucleons is small compared to Λ_b, χEFT aims to provide a model-independent and systematically improvable description of nuclear interactions and observables.

Weinberg power counting in χEFT organizes the most general nuclear Hamiltonian that is consistent with all symmetries of low-energy QCD in powers of $Q = \max\{m_\pi, p\}/\Lambda_b$, where p is a typical momentum associated with the interacting nucleons (soft scale) and Λ_b the momentum at which the χEFT expansion breaks down (hard scale) because the details of the short-distance interaction become relevant [19–22]. If $p < \Lambda_b$, χEFT calculations can (in principle) be improved up to the desired accuracy by working to higher orders; and the residual uncertainties due to truncation of the χEFT expansion at finite order can be quantified. The convergence of the χEFT has been studied in detail in the context of free-space NN scattering using Bayesian methods [59, 60]. These studies indicate that $\Lambda_b \approx 600\,{\rm MeV}$—consistent with the phenomenological expectation that vector mesons such as the $\rho-$meson with mass $m_\rho \simeq 770\,{\rm MeV}$ contribute to nuclear forces at short distances.

In dense matter, the typical momentum scale associated with nuclear interactions will in general depend on the nature of the ground state. When interactions are not too strong, the ground state is expected to resemble a Fermi liquid, so the typical momentum associated with interactions will be proportional to the Fermi momentum $k_{\rm F} = (6\pi^2 n_{\rm B}/g)^{1/3}$, where $n_{\rm B}$ is the baryon number density and g the spin-isospin multiplicity (see Refs. [42, 43] for details). Thus, with increasing density we should expect the efficacy of the χEFT to diminish as the truncation errors associated with finite order calculations grow.

An important recent development is the consistent quantification and propagation of these EFT truncation errors in the energy per particle and derived quantities in dense matter using Bayesian methods [42, 43]. The many-body calculations used in these studies were conducted order-by-order in the χEFT expansion, which allowed for Bayesian inference of the *a priori* unknown Λ_b in infinite matter by making verifiable assumptions about the χEFT expansion that can be tested using diagnostic tools for model checking [59, 60]. This in turn provides the systematic means to estimate and propagate EFT truncation errors. As noted in the previous section, realistic determinations of both $R_{\rm min}(M)$ and $R_{\rm max}(M)$ depend on the effective boundary ε_0 as well as the pressure of nucleonic matter at $P < P_0$ down to the crust. The χEFT uncertainties will therefore contribute to the uncertainties in $R_{\rm min}(M)$ and $R_{\rm max}(M)$ for an assumed value of ε_0.

In what follows, we describe the results of the many-body calculations, the associated EFT truncation error analysis, and the propagation of theoretical uncertainties used in constructing the EOS of beta-equilibrated NSM.

A. Many-body results for PNM and SNM

The BUQEYE collaboration [41] has recently introduced a novel framework for uncertainty quantification of infinite-matter observables calculated from EFT [42, 43]. In this approach, Gaussian Processes with physics-based hyper-parameters are trained on order-by-order calculations of the EOS as a function of the baryon density and proton fraction. This allows for quantification and propagation of statistically robust uncertainties of the EOS to quantities involving derivatives, while self-consistently accounting for correlations in density and across observables (see Ref. [43] for details). Nowadays, EFT truncation errors dominate these theoretical uncertainties, but many-body approximations, etc., also contribute.

As the framework's first application [42, 43], BUQEYE studied the χEFT convergence of the EOS in the limits of PNM and SNM up to N^{3}LO in the density region $n_{\rm B} \lesssim 2.0\,n_{\rm sat}$. They also inferred posterior distributions for nuclear saturation properties and key quantities for neutron stars: the pressure and speed of sound in PNM, and the nuclear symmetry energy as well as its slope in density.

The statistical analysis indicates that the EOS is strongly correlated, which leads to correlation lengths comparable to the $k_{\rm F}$ associated with $n_{\rm sat}$ in PNM and SNM, respectively. In other words, perturbing the EOS at one point in the density (or the proton fraction) perturbs neighboring points (with respect to the correlation length) as well. Without including these correlations, un-

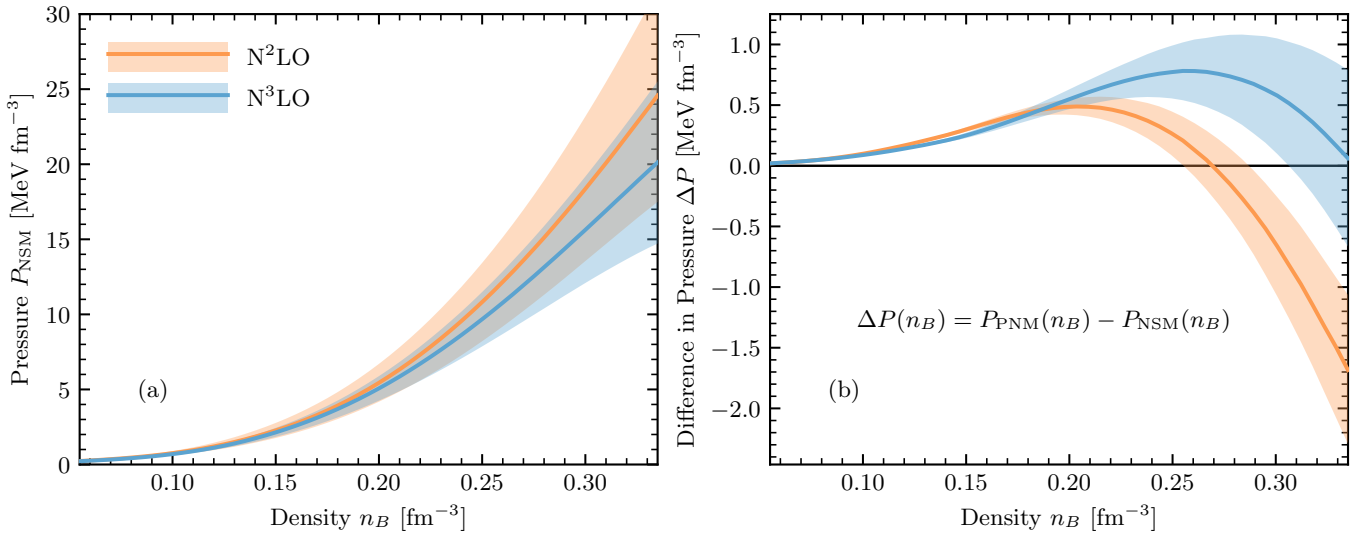

FIG. 2. Panel (a): pressure of neutron-star matter (NSM) as a function of the baryon number density at N^{2}LO (orange-shaded band) and N^{3}LO (blue-shaded band) in the chiral expansion; panel (b): differences of the PNM and NSM pressures as annotated in the panel. The uncertainty bands depict the 1σ confidence region.

certainties in derived quantities of the EOS, such as the nuclear symmetry energy, can be overestimated.

Assuming $p = k_{\rm F}$, the inferred χEFT breakdown scale in PNM and SNM, $\Lambda_b \approx 560 \pm 50\,$MeV, was found to be consistent with free-space NN scattering. If no new degrees of freedom emerge at high densities, this could be associated with $n_{\rm B}(k_{\rm F} = \Lambda_b) = \Lambda_b^3/(3\pi^2) \approx 4.6 \pm 1.2\, n_{\rm sat}$ in PNM, although the χEFT expansion will start losing its predictive power at much lower densities. This should, however, only be considered as a rough estimate (with large uncertainties).

Specifically, BUQEYE's analysis is based on recent order-by-order MBPT calculations in PNM and SNM with chiral NN and 3N interactions up to N^{3}LO [35, 42, 44]. The range in density covers $n_{\rm B} = 0.05 - 0.34\,$fm^{-3}. These calculations significantly improved previous MBPT studies in PNM at N^{3}LO [23, 33, 61], and assessed, for the first time, the SNM EOS with NN and 3N interactions order-by-order up to N^{3}LO. The high-order MBPT calculations were performed by the novel Monte Carlo framework introduced in Ref. [35], which enables MBPT calculations of the EOS with controlled many-body uncertainties for these χEFT interactions.

The underlying nuclear interactions were constrained in Ref. [35] as follows: NN potentials by Entem, Machleidt, and Nosyk [62] up to N^{3}LO were combined with 3N forces at the same order and momentum cutoff so as to construct a set of order-by-order NN and 3N interactions. The two 3N low-energy couplings c_D and c_E, which govern the intermediate- and short-range 3N contributions, respectively, at N^{2}LO were constrained by the triton binding energy and the empirical saturation point of SNM. Several combinations of c_D and c_E with reasonable saturation properties could be obtained at N^{2}LO and N^{3}LO for the momentum cutoffs $\Lambda = 450$ and $500\,$MeV. A momentum cutoff is a typical scale in the regulator function that is applied to χEFT interactions to suppress contributions from high-momentum modes. Note that Λ_b is a physical scale inherent to the EFT, whereas the results should not be sensitive to the artificial scale Λ; in practice, however, this has not yet been achieved in χEFT for infinite matter. The BUQEYE collaboration found that their results do not significantly dependent on which c_D and c_E combination is chosen for a given momentum cutoff. Furthermore, the 3N contributions proportional to c_D and c_E vanish in PNM for nonlocal regulator functions [63]. Consequently, they considered only one combination for each cutoff, and focused their analysis on the Hamiltonian with $\Lambda = 500\,$MeV, while the results for the $\Lambda = 450\,$MeV interaction were provided in the Supplemental Material there.

We follow this strategy here, and note that the residual cutoff dependence is well within the EFT truncation-error estimates at the 1σ level; i.e., for $\Lambda = 450\,$MeV, $P_{\rm PNM}(2.0\, n_{\rm sat}) = 17.29 \pm 4.56\,$MeV fm^{-3} and $E_{\rm PNM}(2.0\, n_{\rm sat}) = 42.86 \pm 5.01\,$MeV, whereas for $\Lambda = 500\,$MeV, $P_{\rm PNM}(2.0\, n_{\rm sat}) = 18.53 \pm 5.14\,$MeV and $E_{\rm PNM}(2.0\, n_{\rm sat}) = 41.55 \pm 5.77\,$MeV fm^{-3}.

BUQEYE's EOSs are given as GPs and publicly available as Jupyter notebooks [41]. A GP is an infinite dimensional generalization of a multi-variate normal distribution, where each point in density is associated with a random variable. Using the Jupyter notebooks we extract the mean values, standard deviations, and correlation information of the energy per particle, pressure, and speed of sound in PNM and SNM, and also the symmetry energy.

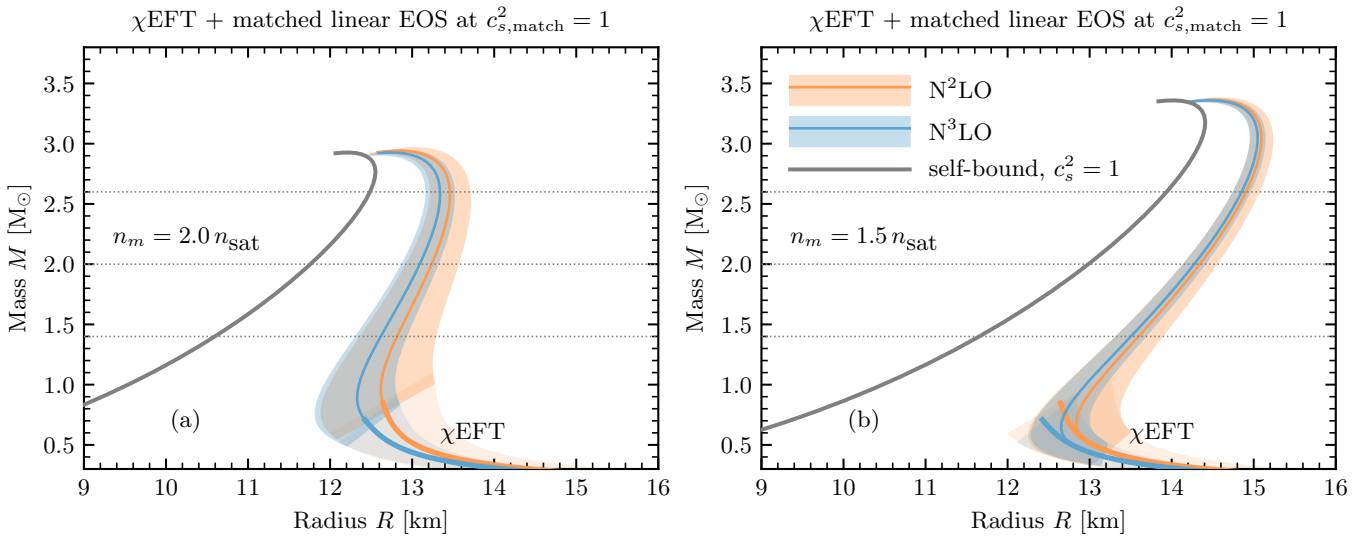

FIG. 3. Panel (a): M–R diagram for NSM based on MBPT calculations shown in Fig. 2 (a), including N^{2}LO-NSM (orange-shaded band) and N^{3}LO-NSM (blue-shaded band) at low densities $\lesssim 2.0\,n_{\mathrm{sat}}$ (both with $\pm 1\sigma$ uncertainties), matched to a linear causal ($c^2_{s,\mathrm{match}} = 1.0$) EOS at $n_{\mathrm{m}} = 2.0\,n_{\mathrm{sat}}$, and the maximally compact EOS for self-bound stars with the same value of M_{max} (black solid). Horizontal lines indicate $M = 1.4,\ 2.0,\ 2.6\,\mathrm{M}_\odot$. The colored bands above $n_{\mathrm{m}} = 2.0\,n_{\mathrm{sat}}$ represent upper bounds on the NS radius for a given mass, as the high-density matter is assumed maximally stiff without discontinuities in the overall EOS (see detailed discussions in Sec. IV C). Panel (b): similar to (a) but with a lower matching density, $n_{\mathrm{m}} = 1.5\,n_{\mathrm{sat}}$.

We consider correlations between the EOSs in PNM and SNM explicitly, neglecting correlations in density. These observables are then given by independent normal distributions sampled on a fine grid in density using the GPs; e.g.,

$$E_{\mathrm{PNM}} \sim \mathcal{N}\left(\mu_{\mathrm{PNM}}, \sigma^2_{\mathrm{PNM}}\right), \tag{14}$$
$$E_{\mathrm{SNM}} \sim \mathcal{N}\left(\mu_{\mathrm{SNM}}, \sigma^2_{\mathrm{SNM}}\right). \tag{15}$$

The nuclear symmetry energy is defined as

$$E_{\mathrm{sym}} = E_{\mathrm{PNM}} - E_{\mathrm{SNM}} \sim \mathcal{N}\left(\mu_{\mathrm{NSM}}, \sigma^2_{\mathrm{NSM}}\right), \tag{16}$$

and, hence, has mean and variance (see, e.g. Ref. [64]):

$$\mu_{\mathrm{sym}} = \mu_{\mathrm{PNM}} - \mu_{\mathrm{SNM}}, \tag{17}$$
$$\sigma^2_{\mathrm{sym}} = \sigma^2_{\mathrm{PNM}} + \sigma^2_{\mathrm{SNM}} - 2\rho\sigma_{\mathrm{PNM}}\sigma_{\mathrm{SNM}}, \tag{18}$$

where ρ is the correlation coefficient between the energies per particle in PNM and SNM. For subsequent discussion, we introduce here also the usual parameters S_v and L in the density expansion of the nuclear symmetry energy Eq. (16),

$$E_{\mathrm{sym}} = S_v + \frac{L}{3}\left(\frac{n_{\mathrm{B}} - n_{\mathrm{sat}}}{n_{\mathrm{sat}}}\right) + \ldots. \tag{19}$$

The correlation between the coefficients in the χEFT expansions for the PNM and SNM energy per particle was quantified to be $\rho^* = 0.934$, corresponding to *very strong* correlations [65, 66]. A detailed discussion can be found in Sec. IV A of Ref. [43]. We have checked that $\rho \simeq \rho^*$ by comparing E_{sym} against the values obtained in Ref. [43]: the maximum deviation between the two approaches is 37 keV (340 keV for its $\pm 1\sigma$ bounds) at the highest density, $n_{\mathrm{B}} = 0.34\,\mathrm{fm}^{-3}$, which is negligible compared to the overall EFT truncation error at that density.

We also found that numerical integration of the pressure of PNM and SNM agreed well with the energy found in the GP approach, the maximum deviation being 3 keV and 1 keV for PNM and SNM, respectively (290 keV and 500 keV for their respective $\pm 1\sigma$ bounds) at the highest density. There are mainly two related reasons why finite differencing for the pressure, discrete integration for the energy, and subtraction for the symmetry energy, works so well. First, the correlation length of the EOS is much longer than the length scale used for finite differencing. That means numerical differentiation follows closely the curves $\mu \pm \sigma$, which are two realizations of the underlying GP. Secondly, the raw EOS data has already been preprocessed by BUQEYE's truncation error model. Numerical noise from the many-body method has been smoothed out, and the EOS has been sampled on a fine grid in density using the GP interpolant. This underlines that GP interpolants are efficient tools for analyzing χEFT calculations of the EOS.

B. Uncertainty propagation to NSM

To construct the EOS of charge-neutral, beta-equilibrated NSM between the crust and $n_{\mathrm{B}} \lesssim 2.0\,n_{\mathrm{sat}}$, we use the standard approximation of keeping only the quadratic term in the nuclear energy expanded in the

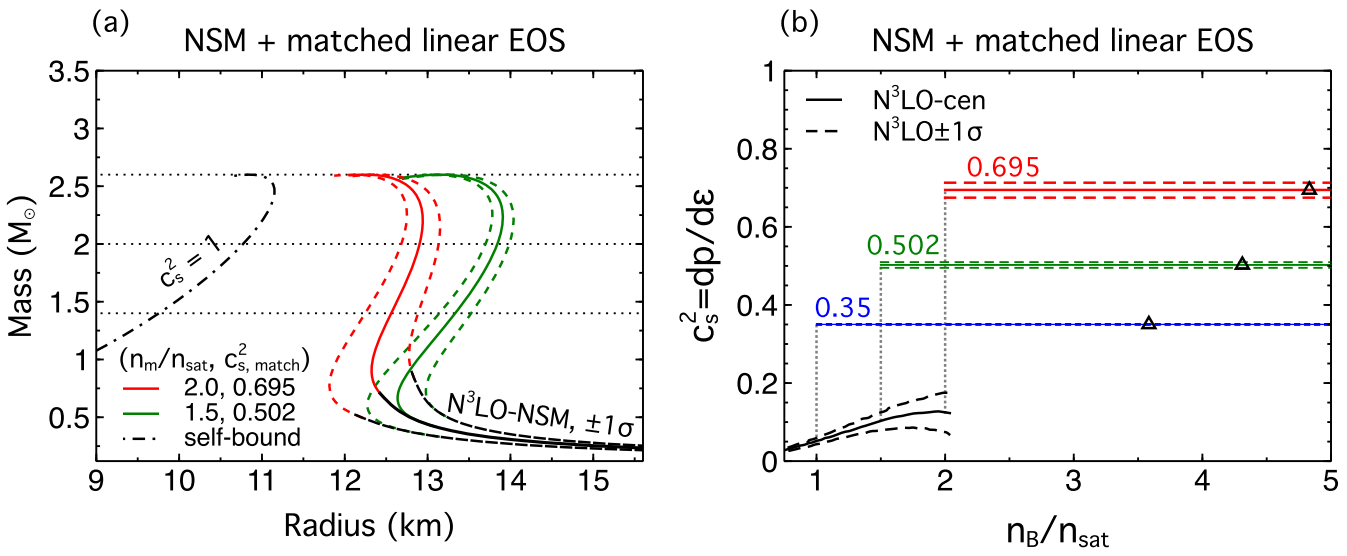

FIG. 4. Panel (a): M–R diagram for matched linear EOSs that give rise to $M_{\rm max} = 2.6\,{\rm M}_\odot$ with N^{3}LO-NSM ($\pm1\sigma$) applied for low densities $\leq 2.0\,n_{\rm sat}$. Corresponding values of $n_{\rm m}$ and $c^2_{s,{\rm match}}$ are indicated. Panel (b): sound speed profiles $c^2_s(n_{\rm B})$ for N^{3}LO-NSM only (black-solid for the central value and black-dashed for $\pm1\sigma$ uncertainties), and matched linear EOSs with different values of $c^2_{s,{\rm match}}$ associated with $M_{\rm max} = 2.6\,{\rm M}_\odot$ in panel (a) (colored horizontal lines). The open triangles mark the central densities of the maximum-mass stars $M_{\rm max} = 2.6\,{\rm M}_\odot$.

isospin asymmetry parameter $\beta = 1-2x$, where $x = n_p/n_{\rm B}$ is the proton fraction, and n_p the proton density. The total energy of NSM is then

$$E_{\rm NSM} = E_{\rm PNM}(1-2x)^2 + E_{\rm SNM}\,4x(1-x) + E_e + E_\mu, \quad (20)$$

where E_e and E_μ are the energies per baryon of electrons and muons, respectively. Microscopic calculations of asymmetric matter based on chiral NN and 3N interactions at $n_{\rm B} \lesssim n_{\rm sat}$ have confirmed that the quadratic expansion Eq. (20) is a reasonable approximation of the full isospin dependence of the EOS [26, 67–70].

Beta equilibrium is the condition that the total charge-neutral energy be minimized with respect to x, or

$$\frac{\partial E_{\rm NSM}}{\partial x} = 0, \quad (21)$$

which is equivalent to

$$\mu_n - \mu_p = 4E_{\rm sym}(1-2x) = \mu_e = \mu_\mu. \quad (22)$$

Here, μ denotes a chemical potential. Propagating the EFT uncertainties to $E_{\rm NSM}$ associated with Eq. (20) is straightforward because of the condition (21). We obtain

$$\sigma^2_{E_{\rm NSM}} = \left(\frac{\partial E_{\rm NSM}}{\partial E_{\rm PNM}}\right)^2 \sigma^2_{E_{\rm PNM}} + \left(\frac{\partial E_{\rm NSM}}{\partial E_{\rm SNM}}\right)^2 \sigma^2_{E_{\rm SNM}} + 2\rho \frac{\partial E_{\rm NSM}}{\partial E_{\rm PNM}} \frac{\partial E_{\rm NSM}}{\partial E_{\rm SNM}} \sigma_{E_{\rm PNM}} \sigma_{E_{\rm SNM}}, \quad (23)$$

with the derivatives $\partial E_{\rm NSM}/\partial E_{\rm PNM} = (1-2x)^2$ and $\partial E_{\rm NSM}/\partial E_{\rm SNM} = 4x(1-x)$.

Figure 2 (a) shows the pressure of NSM (including contributions from the leptons) $P_{\rm NSM} = n_{\rm B}^2(dE_{\rm NSM}/dn_{\rm B})$. The blue (orange) uncertainty band corresponds to the N^{3}LO (N^{2}LO) results at the 1σ level. Panel (b) displays the difference in pressures between PNM and NSM. The zero crossings indicate where the pressure of NSM equals that of PNM. Depending on the chiral order, these crossings occur at $n \approx 1.6-2.1\,n_{\rm sat}$. They are due to a softening of $E_{\rm sym}$ at the higher densities; nevertheless, $E_{\rm NSM}$ is always less than that of $E_{\rm PNM}$. In no case does x exceed about 0.055 for $n_{\rm B} \leq 0.34\,{\rm fm}^{-3}$.

IV. RESULTS

A. NSM and the role of χEFT inputs

In order to compute bounds on NS masses and radii, we assume a typical crust EOS [57, 58] below $0.5\,n_{\rm sat}$ and the EOS for NSM based on MBPT-χEFT calculations [43] up to $n_{\rm m} = 1.0-2.0\,n_{\rm sat}$, and then match to a linear EOS Eq. (9) characterized by c_s^2 at higher densities.

Figure 3 (a) shows the M–R relation for N^{3}LO-NSM, N^{2}LO-NSM EOSs in Fig. 2 (a) matched at $n_{\rm m} = 2.0\,n_{\rm sat}$ to the stiffest linear EOS that with $c_s^2 = 1$; the solid colored curves refer to the central values and the color-shaded bands refer to $\pm1\sigma$ uncertainties in the MBPT-χEFT calculations. Results for matching at a lower density $n_{\rm m} = 1.5\,n_{\rm sat}$ are shown in Fig. 3 (b). As expected, for a given value of $n_{\rm m}$, the largest radii result from the

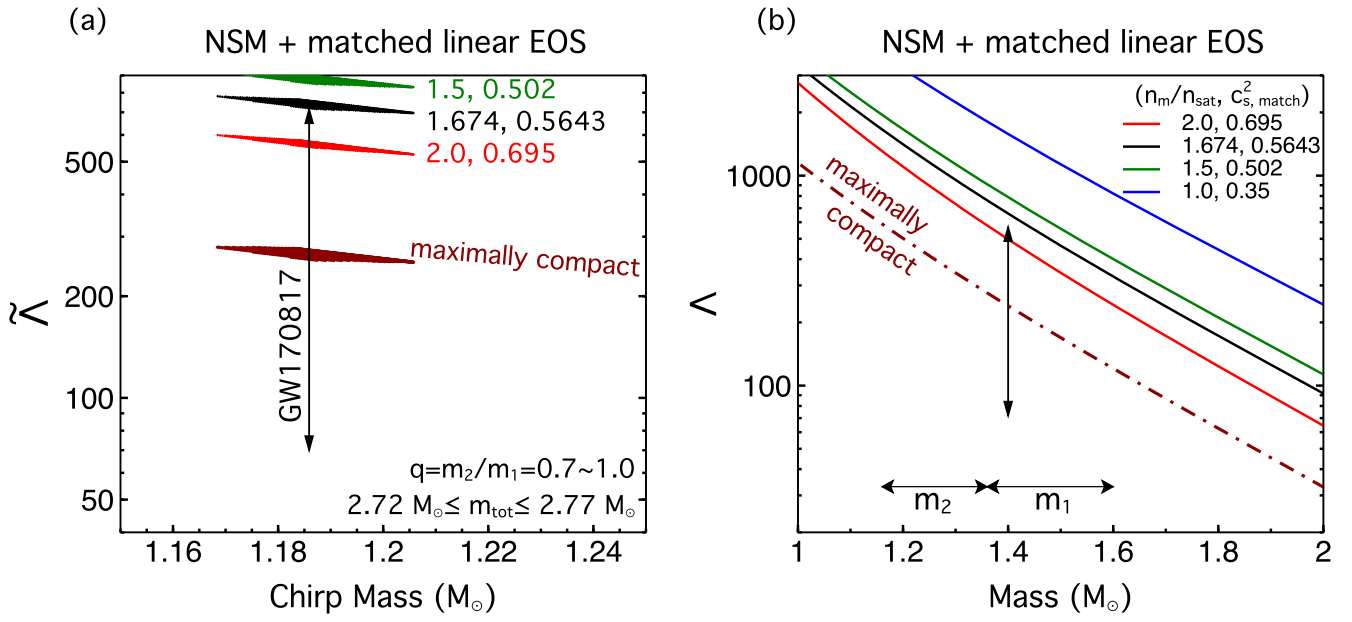

FIG. 5. $\tilde{\Lambda}$–$\mathcal{M}$ and Λ–M relations confronted with constraints from GW170817 [6, 7] (vertical lines with arrows), with fixed $M_{\rm max} = 2.6\,{\rm M}_\odot$ as an example. Parameters for matched EOSs are the same as in Fig. 4, except for the special case with $n_{\rm m} = 1.674\,n_{\rm sat}$ (with $c^2_{s,{\rm match}} = 0.5643$), which refers to the minimum matching density that survives $\tilde{\Lambda}(\mathcal{M} = 1.186\,{\rm M}_\odot) \leq 720$.

largest matching pressure $P_{\rm m}$, and thus N^{2}LO $+1\sigma$, while N^{2}LO-1σ shows little difference compared to N^{3}LO-1σ; here $-\sigma$ ($+\sigma$) refers to the lower (upper bound) on $P(n_{\rm B})$ in Fig. 2. In general, the lower the matching density $n_{\rm m}$, the larger the maximum radii. Any discontinuities in the energy density, such as from a phase transition, would serve to decrease $R(M)$, emphasizing the results in these figures as being upper bounds (see Sec. II). It can be seen that upper bounds on $R_{1.4}$ (where the bands intersect with the $M = 1.4\,{\rm M}_\odot$ horizontal line) of about 12.9 km (13.6 km) result if $n_{\rm m} = 2.0\,n_{\rm sat}$ ($n_{\rm m} = 1.5\,n_{\rm sat}$). We defer a detailed discussion on the radius bounds to Sec. IV C. Self-bound (crustless) stars with $c_s^2 = 1$ for a given $M_{\rm max}$ represent the "maximally compact" configurations that exhibit the smallest possible radii at all masses, and for comparison their mass-radius relations are also displayed (black solid curves).

The overall matched EOSs $\varepsilon(P)$ are continuous but their sound speeds are not, and the causal limit $c_s^2 = 1$ leads to maximum masses as high as $\approx 2.93\,{\rm M}_\odot$ for $n_{\rm m} = 2.0\,n_{\rm sat}$ and $\approx 3.36\,{\rm M}_\odot$ for $n_{\rm m} = 1.5\,n_{\rm sat}$ (differences at low densities, e.g., between N^{3}LO and N^{2}LO have negligible effects on $M_{\rm max}$, as already noted in Sec. II). For a given value of $c^2_{s,{\rm match}}$, $M_{\rm max}$ is essentially determined by $n_{\rm m}$ and is relatively insensitive to $P_{\rm m}$. With smaller (and constant) values of $c^2_{s,{\rm match}}$, the maximum mass decreases.

It is therefore of interest to examine what matching conditions relating $n_{\rm m}$ and $c^2_{s,{\rm match}}$ ensue from a restriction such as $M_{\rm max} = 2.6\,{\rm M}_\odot$. Fig. 4 (a) depicts the M–R relations for $n_{\rm m}$ and $c^2_{s,{\rm match}}$ that lead to $M_{\rm max} = 2.6\,{\rm M}_\odot$, and the corresponding c_s^2 profiles are explicitly shown in panel (b). The required values of $c^2_{s,{\rm match}}$ are indicated in the plot (solid horizontal lines for the N^{3}LO-central (denoted as N^{3}LO-cen) and dashed for $\pm1\sigma$ uncertainties), which increase with the matching density $n_{\rm m}$. At fixed matching density indicated by the vertical dotted lines, the variation in $c^2_{s,{\rm match}}$ above $n_{\rm m}$ is consistent with the uncertainties in c_s^2 from χEFT calculations at $n_{\rm m}$, and a softer EOS (smaller c_s^2) at low densities is compensated by a stiffer EOS (larger $c^2_{s,{\rm match}}$) at higher densities.

The simple linear parametrization of high-density EOS used here can be viewed as a guide to assess the stiffness required at higher densities to achieve $M_{\rm max} \geq 2.6\,{\rm M}_\odot$. Assuming χEFT-N^{3}LO is valid up to $n_{\rm m} = 2.0\,n_{\rm sat}$ ($1.5\,n_{\rm sat}$), to reach $2.6\,{\rm M}_\odot$ the "averaged" c_s^2 above $2.0\,n_{\rm sat}$ ($1.5\,n_{\rm sat}$) has to be greater than ~ 0.7 (~ 0.5). This is probably not achievable by using standard extrapolations of nonrelativistic nucleonic models (for which c_s^2 is gradually increasing) without violating causality below the central density of the maximum mass star. On the other hand, the low-density behavior of the EOS controls predictions on the radii and tidal deformabilities of canonical-mass neutron stars $1.1-1.7\,{\rm M}_\odot$, for which various astrophysical and gravitational-wave constraints are available. The relatively soft N^{3}LO EOS up to $2.0\,n_{\rm sat}$ guarantees that the typical NS radius $\lesssim 13$ km, even with very stiff matter at higher densities ($c^2_{s,{\rm match}} \approx 0.7$ when above $2.0\,n_{\rm sat}$) that leads to $M_{\rm max} \approx 2.6\,{\rm M}_\odot$; see red curves in Fig. 4 (a).

Calculations of tidal deformabilities [71–73] are confronted with the constraints inferred from GW170817 [5–

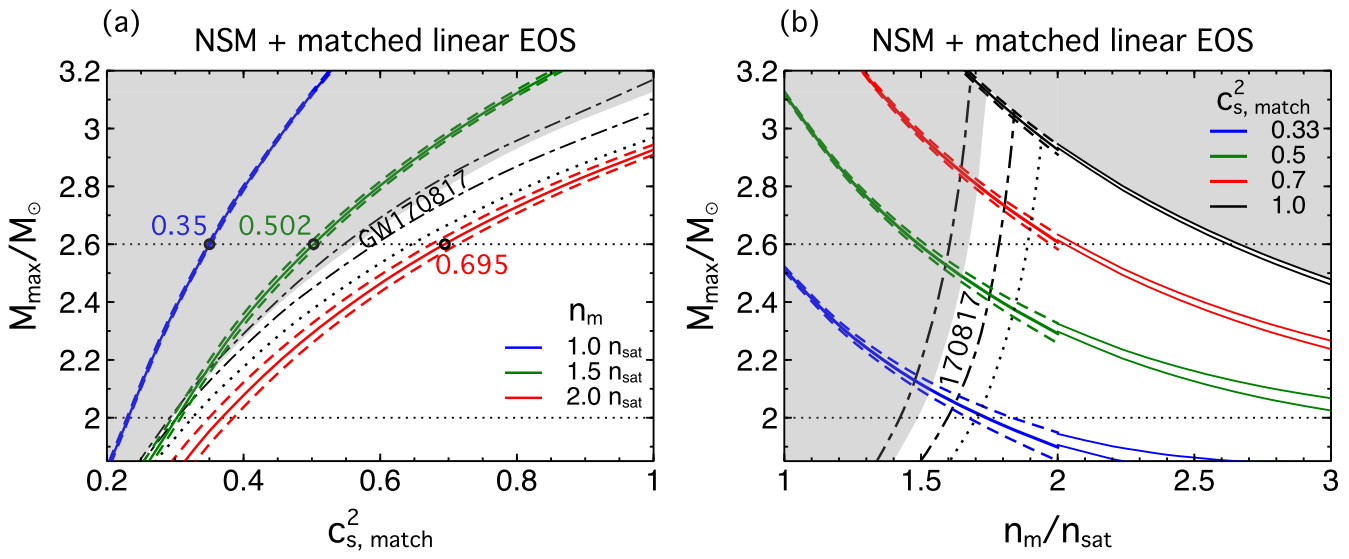

FIG. 6. Panel (a): the solid lines show contours of $n_{\rm m}$ in the $M_{\rm max}$–$c^2_{s,{\rm match}}$ plane, and the dashed lines bracket N^{3}LO $\pm1\sigma$ uncertainties. The upper horizontal line indicates $M_{\rm max} = 2.6\,{\rm M}_\odot$; see also examples in Fig. 4. The grey-shaded region is excluded by the binary tidal deformability constraint $\tilde{\Lambda}_{1.186} \leq 720$ from GW170817 at the 90% crediblitiy level [6] if N^{3}LO-cen is assumed; the dot-dashed lines refer to constraints with the N^{3}LO $\pm1\sigma$ boundaries. The thin dotted line indicates a lower upper bound with N^{3}LO-cen and $\tilde{\Lambda}_{1.186} \leq 600$. Panel (b): same as panel (a), except that contours of $c^2_{s,{\rm match}}$ are displayed in the $M_{\rm max}$–$n_{\rm m}$ plane; the upper-right grey-shaded region is excluded by causality. For $n_{\rm m} \in [2.0, 3.0]\,n_{\rm sat}$, extrapolations from χEFT using ZL models with $L = 50\,{\rm MeV}$ and $L = 60\,{\rm MeV}$ are applied (see Fig. 7).

7] in Fig. 5. Gravitational waveform fitting using the standard PhenomPNRT model [6, 74] directly sets constraints on the binary chirp mass $\mathcal{M} = 1.186 \pm 0.001\,{\rm M}_\odot$ and the tidal deformability $\tilde{\Lambda} \leq 720$ (90% credibility). In what follows, we will denote the constraint on $\tilde{\Lambda}$ at $\mathcal{M}$ as $\tilde{\Lambda}_{1.186} \leq 720$. As mentioned before, a small matching density $n_{\rm m}$ results in a large radius for a given $c^2_{s,{\rm match}}$. An EOS stiffening drastically from N^{3}LO below $1.5\,n_{\rm sat}$ ends up violating $\tilde{\Lambda}_{1.186} \leq 720$ if $M_{\rm max} \gtrsim 2.6\,{\rm M}_\odot$ (green band in Fig. 5 (a)). The $\tilde{\Lambda}$–$\mathcal{M}$ constraint can be translated to a constraint on Λ at the mass M, Λ_M, but it is subject to small additional uncertainties from the poorly determined mass ratio q of GW170817 and EOS systematics. Using the quasi-universal EOS relation $\Lambda_1 = q^6\Lambda_2$, which is valid to 10% – 20% for $\mathcal{M} = 1.186\,{\rm M}_\odot$ and $q > 0.7$ [75], one finds

$$\Lambda_M \simeq 2^{6/5}(\mathcal{M}/M)^6\tilde{\Lambda}_{\mathcal{M}}, \qquad (24)$$

valid to a few percent. Even considering the q and EOS uncertainties, one sees that $n_{\rm m} \lesssim 1.5\,n_{\rm sat}$ violates the GW170817 constraint (Fig. 5 (b)). There exists a minimum $n_{\rm m} \approx 1.7\,n_{\rm sat}$ for N^{3}LO-NSM to survive the $\tilde{\Lambda} \leq 720$ constraint (when $M_{\rm max} \geq 2.6\,{\rm M}_\odot$ is assumed), and an even smaller upper bound e.g., $\tilde{\Lambda} \simeq 600$ [76–78] which would increase the minimum required $n_{\rm m}$. It is noteworthy that the posteriors of $\tilde{\Lambda}$ for GW170817 suggest a peak value around ≈ 225, noticeably smaller than the upper bound of 720 (90% credible level).

A more conservative estimate for the maximum mass, such as $2.2 - 2.3\,{\rm M}_\odot$, increases the allowed range for $n_{\rm m}$ and $c^2_{s,{\rm match}}$ to be consistent with data; the generic trend is shown in Fig. 6. Specifically, Fig. 6 (a) demonstrates how $M_{\rm max}$ scales with $c^2_{s,{\rm match}}$ using the N^{3}LO-NSM EOS for $n_{\rm m} = 1.0, 1.5, 2.0\,n_{\rm sat}$. The solid curves correspond to results for N^{3}LO-cen and the dashed ones with $\pm1\sigma$ uncertainties. The dots indicate the intersections of the central curves with $M_{\rm max} = 2.6\,{\rm M}_\odot$ for the same EOSs as in Fig. 4 (b). The χEFT uncertainties at the respective densities only slightly broaden these correlations. Together with GW170817, the constraint $M_{\rm max} \geq 2.1\,{\rm M}_\odot$ rules out very weakly-interacting matter ($c_s^2 \approx 0.33$) at high densities, whereas $M_{\rm max} \geq 2.5\,{\rm M}_\odot$ rules out matter with $c_s^2 \lesssim 0.5$.

It is worth noting that the GW170817 boundary (edge of the grey-shaded region) for N^{3}LO-cen is nearly parallel to the $n_{\rm m}$ contours. The dot-dashed lines bracket $\pm1\sigma$ uncertainties in N^{3}LO, and the softer N^{3}LO-1σ (stiffer N^{3}LO $+1\sigma$) corresponds to the upper (lower) boundary. This feature is more clearly displayed in panel (b), where $M_{\rm max}$ is plotted against $n_{\rm m}$ for fixed values of $c^2_{s,{\rm match}}$. For matching densities $\lesssim 1.5 - 1.8\,n_{\rm sat}$, all constructed EOSs result in $\tilde{\Lambda}_{1.186} > 720$ and can be therefore considered ruled out by GW170817 (see also examples in

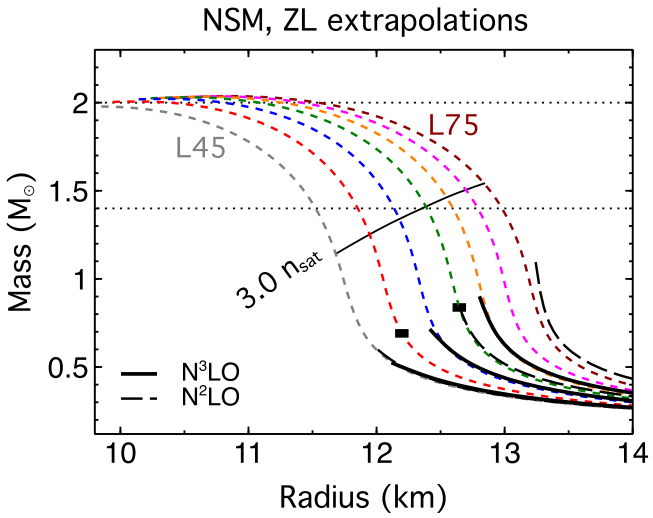

FIG. 7. M–R relations for EOSs extrapolated to high densities beyond the χEFT calculations using the ZL parametrization [79] for NSM at $n_{\rm B} \geq 2.0\,n_{\rm sat}$; the thin black line indicates where the NS central densities are $3.0\,n_{\rm sat}$. From left to right, the colored, dotted curves represent $L = 45\,{\rm MeV}$ to $L = 75\,{\rm MeV}$ in increments of 5 MeV, and the black-solid (black-dashed) curves refer to χEFT-N^{3}LO (N^{2}LO), including $\pm 1\sigma$ uncertainties, up to $\sim 2.0\,n_{\rm sat}$. The $L = 50\,{\rm MeV}$ (red) and $L = 60\,{\rm MeV}$ (green) ZL EOSs are used in Fig. 6 to investigate the trend of $M_{\rm max}(n_{\rm m})$ scaling relations for matching densities between $2.0\,n_{\rm sat}$ (marked with horizontal boxes) and $3.0\,n_{\rm sat}$.

Fig. 5 (a)). If an even lower upper bound on $\tilde{\Lambda}_{1.186}$ were to be established, the excluded region would become larger, increasing the threshold of minimally allowed $n_{\rm m}$.

Compatibility with GW170817 is readily satisfied if the χEFT calculations (with uncertainties) are assumed valid up to $2.0\,n_{\rm sat}$ consistent with previous studies [80]. The evolution of $M_{\rm max}$ with $c^2_{s,{\rm match}}$ has been known [56, 81–83], but it was unclear how the uncertainty in the low-density EOS translates to an uncertainty in the derived upper bound. As shown in Fig. 6 (b), we find that for $n_{\rm m} = 2.0\,n_{\rm sat}$, the uncertainty in $M_{\rm max}$ ranges from $\approx 0.1\,{\rm M}_\odot$ for $c^2_{s,{\rm match}} = 0.33$ (blue-dashed line) to $\approx 0.05\,{\rm M}_\odot$ for $c^2_{s,{\rm match}} = 1$ (black-dashed line) with N^{3}LO $\pm\,1\sigma$ inputs at low densities.

Extrapolating the χEFT EOS to densities somewhat higher than $2.0\,n_{\rm sat}$ will be useful for the subsequent discussion. We find that the ZL parametrization [79] of NSM matter, which has a single parameter corresponding to the symmetry energy coefficient L, is a convenient extrapolation tool. Figure 7 shows M–R curves for the ZL EOSs together with a standard crust. For example, $L = 45\,{\rm MeV}$ (65 MeV) successfully tracks N^{3}LO, while $L = 45\,{\rm MeV}$ (75 MeV) tracks N^{2}LO, for $-\sigma$ ($+\sigma$).

Using the ZL parametrization, we show the consequences of extending the nucleonic EOS to $3.0\,n_{\rm sat}$ in Fig. 6 (b). We find that the ZL EOSs corresponding to $L = 60\,{\rm MeV}$ and 50 MeV, respectively, smoothly join the $M_{\rm max}(n_{\rm m})$ relations for the N^{3}LO $+1\sigma$ and N^{3}LO-cen EOSs[2]; the reason is that the masses of stars with central density $n_{\rm cent} = 2.0\,n_{\rm sat}$ are similar in both cases. The derived bounds on $n_{\rm m}$ and $c^2_{s,{\rm match}}$ illuminate the importance of including nuclear-matter calculations in the density range $1 - 3\,n_{\rm sat}$. Standard extrapolations based on nucleonic models, similar to the ZL parametrization, are usually associated with a more gradual profile of $c^2_s(n_{\rm B})$ at low-to-intermediate densities, which cannot reconcile the small radii and/or small tidal deformabilities inferred for canonical-mass NSs with large maximum masses. The necessary rapid change in the sound speed guided by the simple matching scheme serves to indicate the breakdown of such extrapolations at high densities. A very high NS mass, e.g., $\gtrsim 2.45\,{\rm M}_\odot$ ($2.6\,{\rm M}_\odot$), would be in conflict with causality and standard extrapolation up to $3.0\,n_{\rm sat}$ ($2.66\,n_{\rm sat}$); therefore indicating something unusual in the EOS should should be taking place near this density. This is consistent with the findings of Refs. [45, 46].

It is worth mentioning that so far we have intentionally avoided finite discontinuities in the energy density ε, which would otherwise introduce an additional parameter that characterizes the strength of a sharp first-order phase transition. In that scenario, the $M_{\rm max}$ bounds will be shifted downwards due to the softening induced by the phase transition, while GW170817 boundaries may become more complicated depending on the possible formation of disconnected branches at intermediate densities on the M–R diagram [85, 86]. However, given the systematic uncertainties involved in obtaining $\tilde{\Lambda}$ from gravitational waveform data, the previously inferred bounds should still apply [75]. In any case, as discussed in Sec. II, useful information on the minimal radii $R_{\rm min}(M)$ can be obtained from matching to the causal EOS with a discontinuity $\Delta\varepsilon_{\rm m}$ specified by $M_{\rm max}$, and we will elaborate on these lower bounds on R with χEFT inputs up to $n_{\rm m}$ later in Sec. IV C.

[2] Note that $M_{\rm max}(n_{\rm m})$ for the extrapolated EOSs will eventually bend upwards at sufficiently large $n_{\rm m}$, which is a generic feature whenever a "standard" nucleonic-like EOS (i.e. gradually increasing c^2_s without kinks or discontinuities that naturally extends from low-density e.g. χEFT calculations) is switched to a linear EOS at some critical density, with or without discontinuities in ε (see, e.g., Fig. 5 in Ref. [84]). However, we limit our studies to $n_{\rm m} \lesssim 3.0\,n_{\rm sat}$, as there is little guidance for the validity of nucleonic degrees of freedom at higher densities from theory.

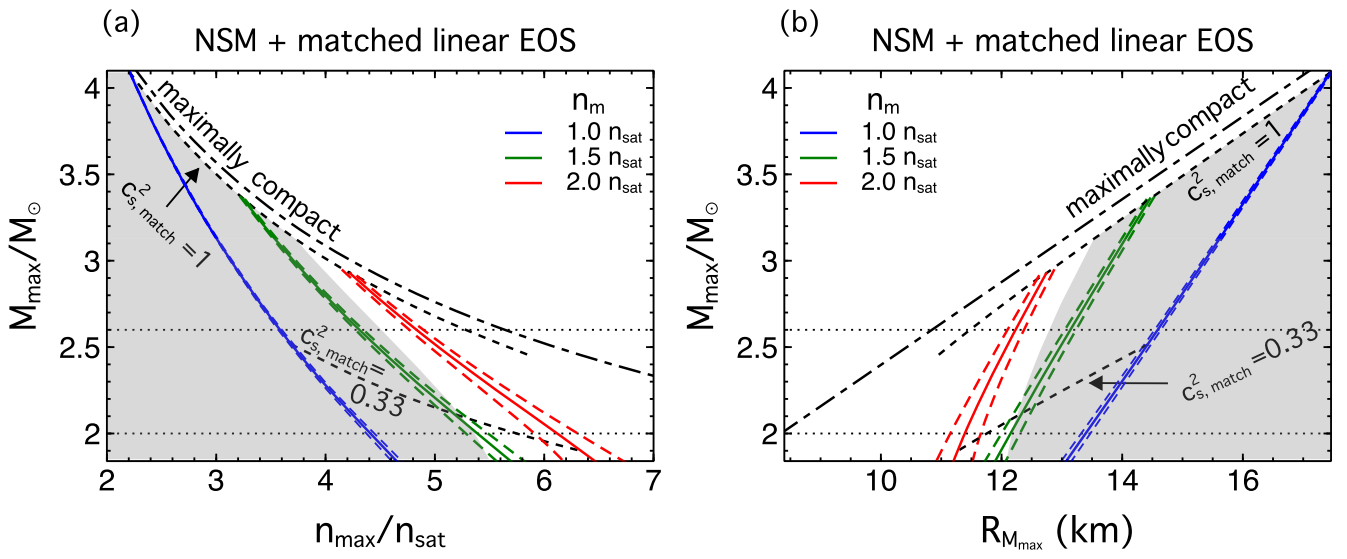

FIG. 8. Panel (a): scaling relations between $M_{\rm max}$ and $n_{\rm max}$; panel (b): scaling relations between $M_{\rm max}$ and $R_{M_{\rm max}}$. Both relations, shown as dot-dashed lines, follow from the maximally compact EOS (see Sec. II). The black dashed curves correspond to the presence of a low-density nuclear mantle (crust + N^{3}LO EOS) for $n_{\rm B} \leq n_{\rm m}$, with fixed sound speeds $c^2_{s,\rm match} = 0.33$ and $c^2_{s,\rm match} = 1.0$ for $n_{\rm B} > n_{\rm m}$. The grey-shaded region is excluded by GW170817 ($\tilde{\Lambda}_{1.186} \leq 720$ and N^{3}LO-cen). The solid colored curves show contours of $n_{\rm m} = 1.0, 1.5, 2.0\, n_{\rm sat}$ for N^{3}LO-cen; dashed colored curves show $\pm 1\sigma$ uncertainties. For EOSs that accommodate $M_{\rm max} \geq 2.6\,{\rm M}_\odot$, the permitted ranges of $n_{\rm max}$ and $R_{M_{\rm max}}$ are severely restricted.

B. Refinements of the limits from the maximally compact EOSs

The "maximally compact" EOSs [53, 56, 87, 88] for self-bound stars with $P_0 = 0$, $P = 0$ for $\varepsilon \leq \varepsilon_0$ in Eq. (1) lead to absolute limits on the central density $n_{\rm max}$ and the radius $R_{M_{\rm max}}$ of the maximum-mass star. In this section, we refine these limits including χEFT uncertainties at low densities and tidal deformability constraints.

In Fig. 8 (a), the dot-dashed boundary represents the absolute upper limit on $M_{\rm max}$ as a function of $n_{\rm max}$, the highest possible baryon density from the maximally compact EOSs; see Eq. (7). The slightly lower black dashed boundary matches the maximally compact EOS to a low-density nuclear EOS at some density $n_{\rm m}$ varying from $n_{\rm sat}$ to about $3.0\,n_{\rm sat}$ (from left to right). The relatively small difference between these two boundaries suggests that effects on the absolute upper bound on $n_{\rm max}$ and $M_{\rm max}$ from the low density EOS is small, and for $M_{\rm max} \geq 2.6\,{\rm M}_\odot$, $n_{\rm max}$ should be smaller than $5.3-5.6\,n_{\rm sat}$. This is in good agreement with $\approx 5\,n_{\rm sat}$ obtained in Ref. [45]. For $n_{\rm m} \leq 2.0\,n_{\rm sat}$, we employ χEFT calculations with uncertainties, and the ZL parametrizations (see Fig. 7) are applied for $n_{\rm m}$ between $2.0-3.0\,n_{\rm sat}$. If the high-density matter is assumed to be much softer with $c^2_{s,\rm match} = 0.33$, matching it to the nuclear EOS at different matching densities $n_{\rm m}$ gives rise to the predicted $M_{\rm max}$–$n_{\rm max}$ relation shown by the lower dashed curve. The grey-shaded region is ruled out by tidal deformability constraints inferred from GW170817, prohibiting small values of $n_{\rm m}$ below $1.5-1.8\,n_{\rm sat}$ (see also Fig. 5). As a result, $c^2_{s,\rm match} \lesssim 0.33$ is incompatible with $M_{\rm max} \gtrsim 2.1\,{\rm M}_\odot$; see also Fig. 6. Furthermore, imposing $M_{\rm max} \geq 2.0\,{\rm M}_\odot$ leads to $5.23 < n_{\rm max}/n_{\rm sat} < 5.79$.

The colored curves in Fig. 8 indicate where the matching densities are fixed at $n_{\rm m}/n_{\rm sat} = 1.0$ (blue), 1.5 (green), and 2.0 (red), and they track decreasing values of $c^2_{s,\rm match}$ from 1 to below 0.33. In each case, the highest $M_{\rm max}$ as well as the smallest $n_{\rm max}$ correspond to where they end at the $c^2_{s,\rm match} = 1$ upper boundary (black dashed line). The N^{3}LO $\pm 1\sigma$ uncertainty at $2.0\,n_{\rm sat}$ translates to $\approx 0.4\,n_{\rm sat}$ uncertainty in $n_{\rm max}$ ($5.9-6.3\,n_{\rm sat}$) if $M_{\rm max} = 2.0\,{\rm M}_\odot$, and $\approx 0.1\,n_{\rm sat}$ uncertainty for $M_{\rm max} = 2.6\,{\rm M}_\odot$. Beyond $n_{\rm m} \gtrsim 2.0\,n_{\rm sat}$, extrapolation of the χEFT calculations is needed for which the curves would move to the lower-right while remaining under the $c^2_{s,\rm match} = 1$ bound. Using the ZL parametrization to extrapolate up to $3.0\,n_{\rm sat}$ (not shown), we obtain $n_{\rm max} \leq 5.71 - 5.92\,n_{\rm sat}$ and $M_{\rm max} \leq 2.45 - 2.48\,{\rm M}_\odot$.

As discussed in Sec. II, the maximally compact EOS with $c^2_s = 1$ determines the smallest possible radius at a given mass. Figure 8 (b) displays the absolute bound on the radius of the maximum mass star, $R_{M_{\rm max}}$, as well as a more realistic bound taking into account the low-density EOS below $n_{\rm m}$. Assuming χEFT up to $n_{\rm m} = 2.0\,n_{\rm sat}$ and $M_{\rm max} = 2.0\,{\rm M}_\odot$, the N^{3}LO $\pm\,1\sigma$ uncertainties induce an uncertainty $\approx 0.5\,$km in $R_{M_{\rm max}} = 11.14 - 11.66\,$km. For $M_{\rm max} = 2.6\,{\rm M}_\odot$, an uncertainty $\approx 0.3\,$km is found with

$R_{M_{\rm max}} = 12.09-12.38$ km. Extrapolating to higher densities $n_{\rm m} \gtrsim 2.0\,n_{\rm sat}$, $M_{\rm max} \geq 2.6\,{\rm M}_\odot$ leads to $R_{M_{\rm max}} \geq 11.49$ km. The tidal deformability constraint inferred from GW170817 instead corresponds to limits on the radii of canonical-mass stars. With the simple matching condition used here, that constraint simultaneously rules out too large $R_{M_{\rm max}}$, e.g., $R_{M_{\rm max}} \leq 12.18$ km if $M_{\rm max} = 2.0\,{\rm M}_\odot$ and $R_{M_{\rm max}} \leq 12.79$ km if $M_{\rm max} = 2.6\,{\rm M}_\odot$.

On the other hand, introducing a finite discontinuity in ε would decrease $R_{M_{\rm max}}$ and increase $n_{\rm max}$, but to reach the same $M_{\rm max}$ necessitates the transition density to be smaller than the matching density $n_{\rm m}$ when there is no discontinuity [89]. The overall effect is that larger $n_{\rm max}$ and smaller $R_{M_{\rm max}}$ are possible but must still lie within the bounds set by the maximally compact EOSs.

C. Bounds on the neutron star radius and tidal deformability

Here, we address how a specification of the nuclear EOS up to $\sim 2.0\,n_{\rm sat}$ including EFT uncertainties, provides robust upper and lower bounds on the radius of a NS of any mass. As we discuss below, these bounds are insensitive to the details of dense matter physics beyond the densities accessible by χEFT.

Earlier work has shown that the radii of canonical NSs with masses in the range $1.2-1.4\,{\rm M}_\odot$ are most sensitive to the EOS in the density interval $1.5-3.0\,n_{\rm sat}$ [2], and this is further quantified in Sec. IV D. As a result, calculations up to $\lesssim 2.0\,n_{\rm sat}$ are adequate to place stringent bounds on the NS radius [1, 80, 90]. These studies combined information about the EOS at $n_{\rm B} \lesssim 2.0\,n_{\rm sat}$ and observational evidence for NSs with mass $M \gtrsim 2.0\,{\rm M}_\odot$ to derive bounds on the radius of NSs in the observed mass range. Here, we follow a similar procedure but with N^{3}LO-χEFT EOS and its associated EFT truncation-error estimates discussed in Sec. III. The upper bound on the radius is obtained by matching smoothly both the energy density and pressure to the maximally stiff EOS with $c_s^2 = 1$ at $2.0\,n_{\rm sat}$. This gives an M–R relation with $M_{\rm max} \simeq 2.9\,{\rm M}_\odot$, as predicted by Eq. (4) with $\varepsilon_0 \simeq 2\,\varepsilon_{\rm sat}$.

The minimum radius is determined by introducing a finite discontinuity in the energy density $\Delta\varepsilon_{\rm m}$ at $n_{\rm m}$ that produces a specified value of $M_{\rm max}$. Above the density $\varepsilon_{\rm m}+\Delta\varepsilon_{\rm m}$, the EOS is assumed to be the causal EOS with $c_s^2 = 1$, and the EOS below the density $\varepsilon_{\rm m}$ is assumed to be the original χEFT EOS. If the pressure at $n_{\rm m}$ was vanishingly small, this would effectively give the $R_{\rm min}(M)$ relation for the maximally compact EOS of self-bound stars as described in Sec. II but with $\varepsilon_0 = \varepsilon_{\rm m} + \Delta\varepsilon_{\rm m}$. With finite pressure at $n_{\rm m}$ based on χEFT calculations, $R_{\rm min}(M)$ will be larger and defines the minimum radii for normal NSs. The magnitude of the discontinuity $\Delta\varepsilon_{\rm m}$ at the matching point $n_{\rm m}$ would then be determined solely by the maximum mass according to Eq. (4). For $M_{\rm max} = 2.0\,{\rm M}_\odot$, we find that $\Delta\varepsilon_{\rm m} \approx \varepsilon_{\rm nuc}(n_{\rm m}) \simeq 2\,\varepsilon_{\rm sat}$ where $\varepsilon_{\rm nuc}(n_{\rm m})$ is the energy density in the nuclear-matter phase calculated using χEFT. To accommodate a maximum mass of $2.6\,{\rm M}_\odot$ requires a much smaller discontinuity, $\Delta\varepsilon_{\rm m} \approx 0.25\,\varepsilon_{\rm nuc}(n_{\rm m})$. Furthermore, all the trajectories within any $\pm 2\sigma$ band for each value of $M_{\rm max}$ have nearly identical values of $\Delta\varepsilon_{\rm m}$ resulting from the fact that $P_{\rm m} \ll \varepsilon_{\rm m}$. Thus the relation between $\Delta\varepsilon_{\rm m}$ at $2.0\,n_{\rm sat}$ and $M_{\rm max}$ is indeed relatively insensitive to the low-density EOS.

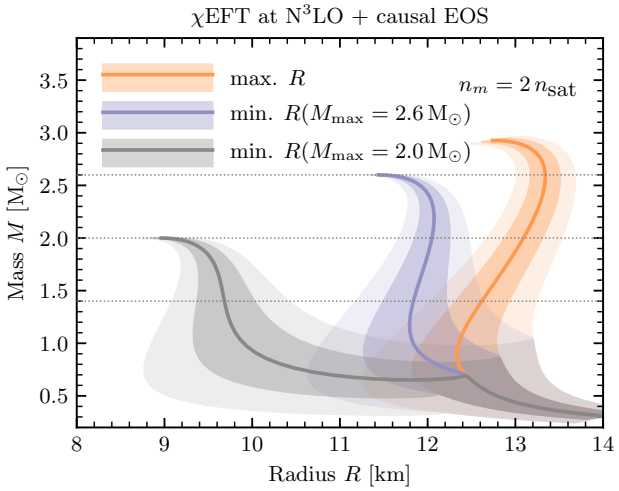

FIG. 9. Radius bounds obtained by combining N^{3}LO-χEFT predictions up to $n_{\rm m} = 2.0\,n_{\rm sat}$ and maximum-mass information is shown. The orange bands show the upper bound on the NS radius, while the black and purple bands depict the lowers bounds corresponding to $M_{\rm max} = 2.0\,{\rm M}_\odot$ and $M_{\rm max} = 2.6\,{\rm M}_\odot$, respectively.

Figure 9 shows the minimum radius and maximum radius bounds. The central values of the minimum radii $R_{\rm min}(M)$ for $M_{\rm max} = 2.0\,{\rm M}_\odot$ and $M_{\rm max} = 2.6\,{\rm M}_\odot$ are shown as black and purple solid curves, respectively, while the darker and lighter bands reflect 1σ and 2σ uncertainties, respectively. To 2σ confidence, the minimum radius of a $1.6\,{\rm M}_\odot$ star ranges from $9.2-12.2$ km as $M_{\rm max}$ is varied from $2.00\,{\rm M}_\odot$ to $2.93\,{\rm M}_\odot$; roughly, the minimum value of $R_{1.6} \propto M_{\rm max}^{3/4}$. Similarly, the minimum values of $R_{M_{\rm max}}$ vary from $9.0-12.6$ km. It is interesting to compare these results with claims that $R_{1.6} > 10.68$ km and $R_{M_{\rm max}} > 8.6$ km from observations of GW170817 [91] using empirical relations established in hydrodynamical simulations that relate R, $M_{\rm max}$, and the threshold binary mass $M_{\rm thres}$ for prompt collapse of a merger remnant. We can therefore provide a more restrictive bound for $R_{M_{\rm max}}$ since $M_{\rm max}$ is believed to be $\geq 2.0\,{\rm M}_\odot$.

The maximum radius curves in Fig. 9 are identical to those presented in Fig. 3 (a). Figure 9 demonstrates how future discoveries of NSs with large masses can constrain the radii of all NSs. Several interesting insights can be gleaned from this figure. A striking, albeit expected, feature is the convergence of the upper and lower radius bounds with increasing $M_{\rm max}$. This is in accordance with the facts that the discontinuity $\Delta\varepsilon_{\rm m}$ leading to the mini-

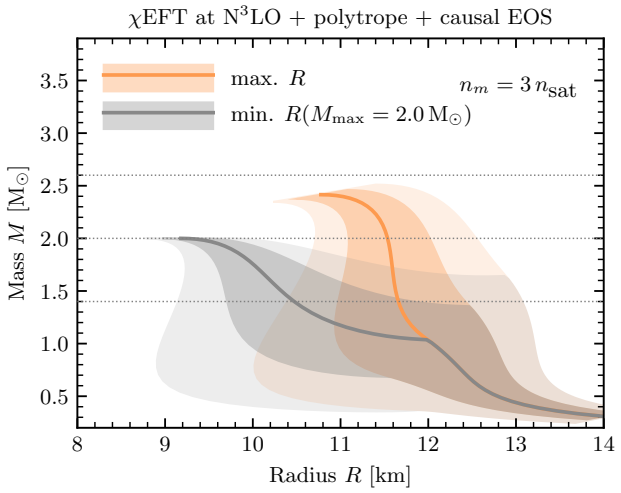

FIG. 10. Similar to Fig. 9 but obtained using the polytropic extrapolation of the χEFT EOS up to $n_{\rm m} = 3.0\,n_{\rm sat}$.

mum radii has to decrease to achieve a higher $M_{\rm max}$ [84] and that the limit $\Delta\varepsilon_{\rm m} \to 0$ defines the maximum radii. For example, the uncertainty in theoretical predictions for the radius of a $1.4\,{\rm M}_\odot$ NS would be reduced from about 3 km when $M_{\rm max} = 2.0\,{\rm M}_\odot$ to about 0.5 km when $M_{\rm max} = 2.6\,{\rm M}_\odot$. Another feature worth noting is the evolution of the 2σ lower bound on the NS radius. It increases by about 2 km, from 9.2 km for $M_{\rm max} = 2.0\,{\rm M}_\odot$ to 11.2 km when $M_{\rm max} = 2.6\,{\rm M}_\odot$. Comparing the black and purple bands shows that the radii of heavier neutron stars are even more tightly constrained with increasing $M_{\rm max}$. Future observational constraints on NS radii in the mass range $1.4-2.0\,{\rm M}_\odot$ could be valuable in this regard since X-ray and GW observations are best suited to provide radius information at the level of 5% uncertainty in this mass range [92]. Results in Fig. 9 also demonstrate that an upper bound of about 13 km for $R_{1.4}$ obtained from GW170817 is consistent with NSs with $M_{\rm max} \simeq 2.6\,{\rm M}_\odot$.

The trends seen in Fig. 9 also have important implications for the EOS of matter at the highest densities encountered in the NS inner core. Our results imply that $M_{\rm max} > 2.5\,{\rm M}_\odot$ and/or radii > 12.5 km for neutron-star masses $\simeq 1.4\,{\rm M}_\odot$ can only be achieved if $c_s^2 \simeq 1$ over a wide density range encountered in the NS core. We emphasize here that this insight relies on the relatively soft EOS predicted by N^{3}LO-χEFT calculations. Improving the EOS, especially the EFT truncation errors in the vicinity of $n_{\rm B} \simeq 2.0\,n_{\rm sat}$, will be critical in extracting better constraints on the EOS at higher densities in the core if future observations favor these large radii or masses. Supporting $c_s^2 \simeq 1$ from $2-5\,n_{\rm sat}$ requires a form of strongly interacting relativistic matter that poses significant challenges for dense-matter theory and QCD [93].

Encouraged by the apparent convergence of χEFT calculations over the density interval $1-2\,n_{\rm sat}$, it is natural to ask if a nuclear physics based description of dense matter can be extended to higher density. Extrapolating the EOS from $2.0\,n_{\rm sat}$ to $3.0\,n_{\rm sat}$ will be model-dependent, even in the absence of phase transitions to non-nucleonic matter, since we presently do not have reliable calculations at higher densities. We climb this rung of the density ladder with some reservation to motivate and explore the impact of future calculations of the EOS in this density interval.

We consider a polytropic model where $P = \kappa\varepsilon^\gamma$ in which the parameters κ and γ are determined by fitting to the behavior predicted by χEFT calculations in the density interval $1.9-2.1\,n_{\rm sat}$ to extrapolate the EOS from $2.0\,n_{\rm sat}$ to $3.0\,n_{\rm sat}$. This choice is somewhat arbitrary and is chosen to approximately capture the key features of the density dependence of the EOS predicted by χEFT. The resulting radius bounds are shown in Fig. 10. We have checked that alternate extrapolations using the ZL EOSs, with parameters chosen to suitably match the χEFT results at $2.0\,n_{\rm sat}$, do not significantly alter our conclusions.

A comparison between the results shown in Fig. 9 with those in Fig. 10 reveals the following insights. First, the increase in $n_{\rm m}$ does not alter the bounds on $R_{\rm min}(M)$ (including $R_{M_{\rm max}}$), as a function of $M_{\rm max}$, except that in the extrapolated case M and $M_{\rm max}$ cannot exceed about $2.5\,{\rm M}_\odot$. These bounds are therefore particularly robust for $M < 2.5\,{\rm M}_\odot$.

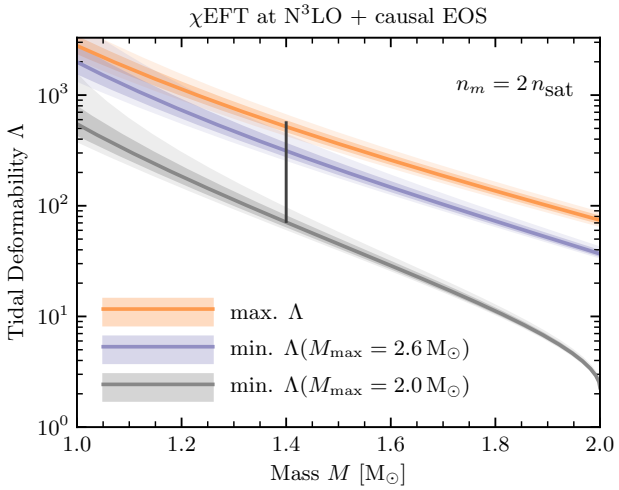

FIG. 11. Bounds on the tidal deformability Λ obtained using χEFT N^{3}LO EOS up to $n_{\rm m} = 2.0\,n_{\rm sat}$. As in Fig. 9, the orange bands show the upper bound, while the lower bounds corresponding to $M_{\rm max} = 2.0\,{\rm M}_\odot$ and $M_{\rm max} = 2.6\,{\rm M}_\odot$ are shown by the black and purple bands, respectively. The vertical solid line depicts the constraint inferred from GW170817, $70 \le \Lambda_{1.4} \le 580$.

Second, the increase in $n_{\rm m}$ results in more stringent upper bounds on the NS radius for masses in the range $1.4-2.5\,{\rm M}_\odot$. For example, the polytropic extrapolation to $3.0\,n_{\rm sat}$ predicts $R_{\rm max}(1.4\,{\rm M}_\odot) = 11.6^{+0.8}_{-0.6}$ km, which is to be contrasted with $R_{\rm max}(1.4\,{\rm M}_\odot) = 12.5^{+0.3}_{-0.2}$ km obtained using $n_{\rm m} = 2.0\,n_{\rm sat}$. This reduction has implications for the interpretation of future radius measurements

which aim for an accuracy of better than 5% [92]. If these observations favor NSs in this mass range to have radii $> 12\,\mathrm{km}$, it would require new mechanisms to rapidly stiffen the EOS below $3.0\,n_{\rm sat}$.

Third, if the secondary component in GW190814 was confirmed to be a massive NS, new mechanisms would also be implicated at a lower density, since the extrapolated EOS up to $3.0\,n_{\rm sat}$ predicts $M_{\rm max}$ in the range $2.32 - 2.53\,\mathrm{M}_\odot$ at $\pm 2\sigma$.

Upper bounds on the tidal deformability Λ can also be derived by smoothly matching the causal EOS to a low-density EOS [94], whereas lower bounds on Λ are determined by matching them to a causal EOS with a discontinuity in the energy density determined by $M_{\rm max}$ [75, 86] (the same procedure used to determine the minimum radius in Figs. 9 and 10). The bounds for the N^{3}LO-χEFT EOS with $n_{\rm m} = 2.0\,n_{\rm sat}$ are shown in Fig. 11. The role of $M_{\rm max}$ is clear from comparison of the $M_{\rm max} = 2.0\,\mathrm{M}_\odot$ and $M_{\rm max} = 2.6\,\mathrm{M}_\odot$ cases.

In Fig. 12 we show the upper and lower bounds obtained by using χEFT up to $2.0\,n_{\rm sat}$ and the polytropic extrapolations from χEFT up to $3.0\,n_{\rm sat}$. The fact that uncertainties in the GW170817 constraint of Λ extend almost precisely between the lower ($M_{\rm max} = 2.0\,\mathrm{M}_\odot$ with a large discontinuity $\Delta\varepsilon_{\rm m}$ at $n_{\rm m}$) and upper bounds ($c^2_{s,\rm match} = 1$ without discontinuity) to within 2σ for both $n_{\rm m} = 2.0\,n_{\rm sat}$ and $n_{\rm m} = 3.0\,n_{\rm sat}$ cases is not a coincidence. It is a consequence of the fact that for those values of $n_{\rm m}$, $\tilde{\Lambda}_{1.186} < 720$ is always satisfied for all values of $c^2_{s,\rm match} \leq 1$ (see Fig. 6).

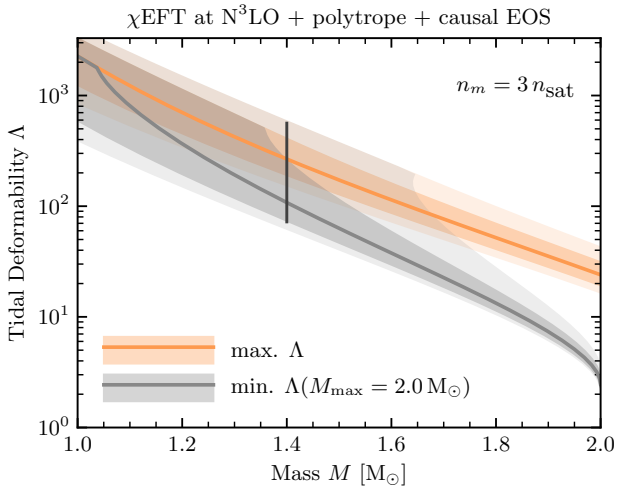

FIG. 12. Upper and lower limits on the tidal deformability as a function of mass based on the extrapolated EOS used in Fig. 10. The vertical solid line depicts the constraint inferred from GW170817, $70 \leq \Lambda_{1.4} \leq 580$.

A comparison between the results shown in Fig. 11 and Fig. 12 provides quantitative insights into how access to the EOS at higher density will impact predictions for the tidal deformability Λ, especially for more massive NSs. It illustrates how constraints on Λ from future GW detections from binaries with massive NSs can provide insights on the evolution of c_s^2 in the density interval $2 - 3\ n_{\rm sat}$. For example, if $\Lambda_{2.0} \gtrsim 100$, it would pose a serious challenge for χEFT predictions even in the density interval $1 - 2\ n_{\rm sat}$, and $\Lambda_{2.0} \gtrsim 50$ would be difficult to accommodate without new mechanisms to significantly stiffen the EOS in the density interval $2 - 3\ n_{\rm sat}$. On the other hand, if $\Lambda_{1.4} \lesssim 100$, it would imply a soft EOS between $1 - 3\ n_{\rm sat}$, a near-causal EOS at higher densities, and $M_{\rm max}$ not significantly larger than $2\,\mathrm{M}_\odot$.

D. Sensitivity to EOS density ranges

It is apparent that the limits to NS radii and tidal deformabilities are sensitive to the EOS in the density range $1-3\,n_{\rm sat}$, precisely where the restrictions from χEFT are important. This is not surprising given the tight correlation between $R_{1.4}$ and the NSM pressure for $1 - 2\,n_{\rm sat}$ discovered by Ref. [2]. However, up to this point, we have assumed fixed sound speeds above $n_{\rm m}$. In this section, we demonstrate that this correlation is insensitive to the details of the assumed EOS at all relevant densities; furthermore, we quantify this correlation and extend it to include the quantities $R_{2.0}$ and $M_{\rm max}$.

We evaluate these correlations by considering several parametrization schemes to construct families of high-density NSM EOSs at densities larger than about $0.5\,n_{\rm sat}$, the assumed core-crust boundary. All configurations are assumed to have a crust modeled with the SLy4 EOS [95]. Each EOS is given as a function of $n_{\rm B}$ only and is implicitly considered to represent beta-equilibrium matter. The parameters for each parametrization scheme are constrained to ensure causality, $c_s^2 \geq 0$, a minimum value $M_{\rm max} = 2.0\,\mathrm{M}_\odot$, a lower limit to the neutron-matter energy and pressure suggested by the unitary-gas conjecture [96] at all supra-nuclear densities, and upper limits to the NSM energy and pressure at $n_{\rm sat}$ implied by experimental limits of $S_v = 36\,\mathrm{MeV}$ and $L = 80\,\mathrm{MeV}$ [97]. Note that the latter two constraints are broader than the NSM-χEFT $\pm 1\sigma$ constraints, so that the correlations we find are conservatively expressed. Also, for each parametrization, we have ensured a minimum of 15,000 realizations that satisfy our constraints. We quantify a correlation in terms of the covariance between two quantities A and B,

$$\mathrm{cov}(A,B) = \sum_{i,j} \frac{(A_i - \bar{A})(B_j - \bar{B})}{\sigma_A \sigma_B}. \qquad (25)$$

The σ's represent standard deviations. We take $A = P(n_{\rm B})$ and $B = R_{1.4}$, $R_{2.0}$, or $M_{\rm max}$. Here, j ranges over all realizations of a given parameterized EOS and i over all values of $n_{\rm B}$ smaller than the central density of the relevant configuration for B.

Figure 13 shows the correlations between the pressure $P(n_{\rm B})$ and $R_{1.4}$, $R_{2.0}$ and $M_{\rm max}$ as functions of the baryon number density $n_{\rm B}$ for a variety of NSM

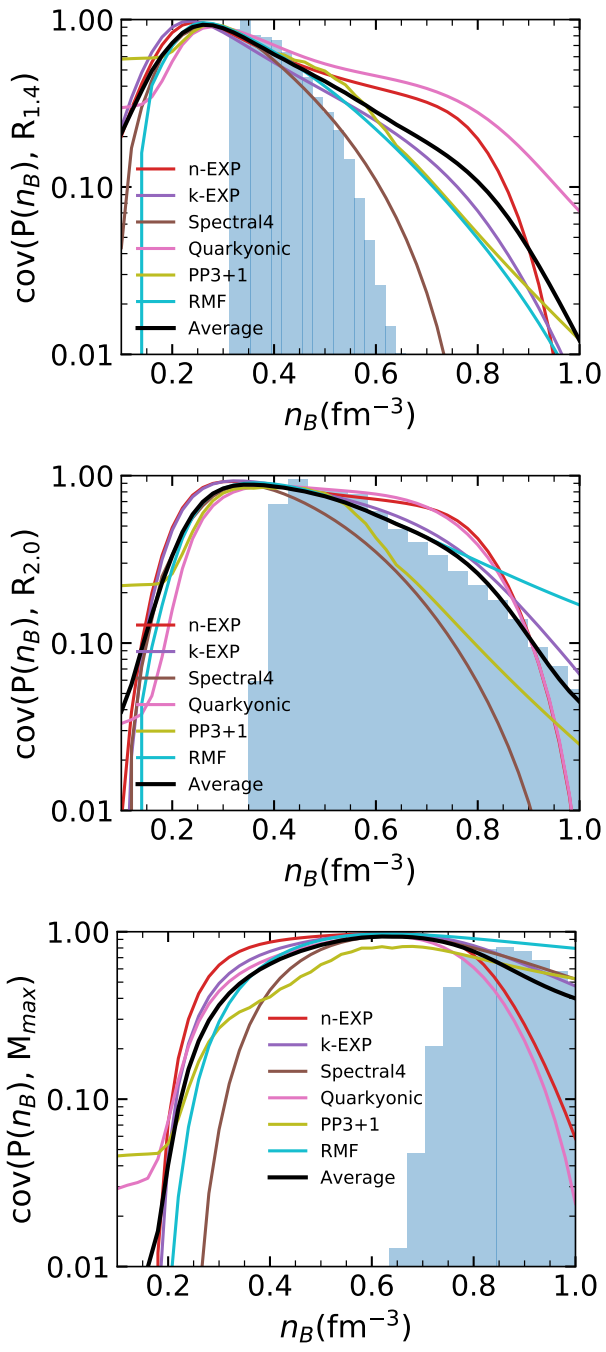

FIG. 13. Correlations among $P(n_{\rm B})$, $R_{1.4}$, $R_{2.0}$ and $M_{\rm max}$ for 6 EOS parametrizations (see text for details). "Average" refers to the mean of all models. Blue histograms show the summed distributions of the central densities of the relevant stars.

parametrizations in common use. The parametrizations "n-EXP" and "k-EXP" are three-parameter Taylor expansions of the NSM energy in terms of $n_{\rm B}$ and $n_{\rm B}^{1/3}$ [96], respectively. "n-EXP" is commonly used to model the nuclear energy around saturation; we take a Taylor expansion up to the fourth-order term $[(n_{\rm B}-n_{\rm sat})/n_{\rm sat}]^4$. Two of the coefficients are set to match the crust EOS, leaving three free parameters. "k-EXP" contains a kinetic term $\propto (n_{\rm B}/n_{\rm sat})^{2/3}$ and a higher-order term up to $(n_{\rm B}/n_{\rm sat})^{7/3}$. It also has three free parameters after using two coefficients to match the crust EOS. ' 'Spectral4" is the four-parameter spectral decomposition method [98–100]. "Quarkyonic" has two parameters, Λ and κ, specifying the quarkyonic momentum shell thickness and the transition density, and one parameter (effectively controlling L) for the nucleon potential [93]. "PP3+1" is a four-parameter piecewise-polytrope with three segments appended to the crust [101]. The density n_1 separating the first two segments is a parameter, while n_2 and n_3 are chosen to scale as $n_2 = 2\,n_1$ and $n_3 = 2\,n_2$. The corresponding bounding pressures P_1, P_2, and P_3 are the other three free parameters[3]. "RMF" is a relativistic mean field model based on the FSU2 EOS [102] and contains σ, ω, and ρ meson exchanges. It has seven coupling constants, of which three are fixed by saturation properties of SNM; the remaining four free parameters can be mapped to S_v, L, the effective nucleon mass at the saturation density, M^*, and the ω self-interaction coupling ζ.

The covariance parameter $\mathrm{cov}(P(n_{\rm B}), R_{1.4})$ peaks around $n_{\rm B} = 1.65^{+1.32}_{-0.68}\,n_{\rm sat}$, whereas $\mathrm{cov}(P(n_{\rm B}), R_{2.0})$ and $\mathrm{cov}(P(n_{\rm B}), M_{\rm max})$ peak around $n_{\rm B} = 2.17^{+2.14}_{-0.81}\,n_{\rm sat}$ and $n_{\rm B} = 3.90^{+2.00}_{-1.81}\,n_{\rm sat}$, respectively. The uncertainties correspond to 50% of the peak covariance. Figure 13 also quantifies the extent to which the central baryon densities, and the width of their distributions, increase with the NS mass. Notably, the central baryon number densities peak at about 30% higher density than do the peak covariance in all three cases, but the widths of the central density distributions rapidly increase with NS mass.

The correlation between the pressure $P(n_{\rm B})$ and $R_{1.4}$ is strongest between $n_{\rm sat}$ and $3.0\,n_{\rm sat}$, as expected, and that between the pressure and $R_{2.0}$ is strongest at about 40% higher densities. Significantly, these results appear to be relatively insensitive to the details of the parametrizations. The standard deviations of both $\mathrm{cov}(P(n_{\rm B}), R_{1.4})$ and $\mathrm{cov}(P(n_{\rm B}), R_{2.0})$ for the six parametrizations are small, being $\sigma_{{\rm cov},R} < 0.2$ for all densities and $\sigma_{{\rm cov},R} < 0.05$ near the covariance peaks. The bottom line is these results demonstrate, at present, that χEFT greatly constrains $R_{1.4}$ and, to a slightly lesser degree, $R_{2.0}$. The situation is somewhat different for $M_{\rm max}$, where pressures at densities between $2.0\,n_{\rm sat}$ and $6.0\,n_{\rm sat}$ dominate. In addition, the standard deviation of $\mathrm{cov}(P(n_{\rm B}), M_{\rm max})$ among the six parametrizations are somewhat larger, being $\sigma_{{\rm cov},M_{\rm max}} < 0.25$ at all densities and $\sigma_{{\rm cov},M_{\rm max}} < 0.1$ near the covariance peak. Thus, the $M_{\rm max}$ results are more model-dependent, and the significant densities likely lie above the validity range for χEFT. However, further refinement of EFT techniques at high densities

[3] The additional parameter n_1 greatly increases the flexibility of PP3+1 compared to the three-parameter (P_1, P_2, P_3) set PP3 often employed [101].

combined with Bayesian uncertainty quantification might change that situation by providing improved constraints on all three quantities, although the EFT truncation error increases rapidly beyond $n_{\rm sat}$.

V. DISCUSSION AND OUTLOOK

A. Current and future constraints

To shed light on the properties of dense matter, the observational constraints used in this work are taken from (i) a handful of well measured NS masses from radio observations [8–12], (ii) the chirp and combined masses as well as bounds on tidal deformabilities of NSs deduced from GW detections in the binary NS-NS merger event GW170817 [5–7], and (iii) radius estimates from NICER for a NS of mass $\simeq 1.4\,{\rm M}_\odot$ [103, 104]. An upper bound of $M_{\rm max} \lesssim 2.3\,{\rm M}_\odot$ on the maximum gravitational mass of a cold, spherical NS was inferred from several studies using EM and GW data from GW170817 [3, 4, 105–107], but an upper bound on $M_{\rm max}$ itself does not provide further limits on the sound speed or bounds to NS radii since the EOS could suddenly soften above $n_{\rm m}$.

The NICER M–R constraints on J0030+0451, namely, $R = 13.02^{+1.24}_{-1.19}\,{\rm km}$, $M = 1.44^{+0.15}_{-0.14}\,{\rm M}_\odot$ [104] and $R = 12.71^{+1.14}_{-1.19}\,{\rm km}$, $M = 1.34^{+0.15}_{-0.16}\,{\rm M}_\odot$ [103], and some EM observations of GW170817 [108–110] favor larger radii than indicated by GW observations from GW170817, $10-13\,{\rm km}$ [6, 7], but the degree of tension is slight. Joint analyses of these data yield tighter but still consistent constraints on the typical NS radius $\sim 12.3\,{\rm km}$ [111–114]; Ref. [115] found $11.8^{+1.0}_{-0.7}\,{\rm km}$ to 68.3% confidence.

It is fortunate that NICER targets also include several pulsars for which the masses are independently measured to high precision, e.g., PSR J1614-2230 $\simeq 1.91\,{\rm M}_\odot$ and PSR J0740+6620 $\simeq 2.14\,{\rm M}_\odot$, and PSR J0437-4715 [116] with mass $\approx 1.44\,{\rm M}_\odot$. The possibility to measure radii of both intermediate as well as very massive NSs opens up the possibility to contrast the radii of $\sim 2.0\,{\rm M}_\odot$ stars, $R_{2.0}$, and more typical $\sim 1.4\,{\rm M}_\odot$ stars, $R_{1.4}$, to further constrain the EOSs [89].

We show in Fig. 14 the difference $\Delta R = R_{2.0} - R_{1.4}$ for stars with the N^{3}LO EOS up to $2.0\,n_{\rm sat}$, ZL EOS extrapolations up to a range of matching densities $n_{\rm m} = 2.0 - 3.0\,n_{\rm sat}$, and various linearly matched EOSs with different $c^2_{s,{\rm match}}$ at higher densities. The ZL extrapolation with $L = 50\,{\rm MeV}$ indicates that roughly above $n_{\rm m} \gtrsim 2.8\,n_{\rm sat}$, all values of $c^2_{s,{\rm match}}$ lead to $R_{2.0} \leq R_{1.4}$. The boundary between positive and negative ΔR shifts a bit when using the slightly stiffer ZL extrapolation with $L = 60\,{\rm MeV}$: in this case $n_{\rm m} \gtrsim 2.6\,n_{\rm sat}$ will guarantee $R_{2.0} \leq R_{1.4}$; note that $2.98\,n_{\rm sat}$ is already the central density of a $1.4\,{\rm M}_\odot$ star. We also checked radii differences between $2.1\,{\rm M}_\odot$ and $1.4\,{\rm M}_\odot$ stars, $\Delta R' = R_{2.1} - R_{1.4}$, and found that $\Delta R'$ is generally less than ΔR, with the largest decreases of a few tenths of a km occurring for the smaller values of $c^2_{s,{\rm match}}$. For $c^2_{s,{\rm match}} \gtrsim 0.7$, there are negligible differences. ΔR or $\Delta R'$ being negative is typical when extrapolations to even higher densities are applied, or if there is additional softening in the EOS before reaching the central density of the maximum-mass star. Should observations suggest $R_{2.0} > R_{1.4}$ or $R_{2.1} > R_{1.4}$, standard extrapolations such as ZL-models predict some unusual stiffening should occur below $\lesssim 2.6 - 2.8\,n_{\rm sat}$. Furthermore, if ΔR turns out to be greater than 0.5 km, then we should expect that this stiffening occurs for $n_{\rm m} \lesssim 2.0\,n_{\rm sat}$, which suggests a very high $M_{\rm max}$ and less compatibility with radius constraints from GW170817; see Fig. 6 (b). However, NICER observations may not achieve the needed $\mathcal{O}(0.5\,{\rm km})$ resolutions in the near future. Since central densities of $\sim 2.0\,n_{\rm sat}$ correspond to $0.5 - 1.0\,{\rm M}_\odot$ within 1σ uncertainties of χEFT calculations (Fig. 9), it will be greatly helpful if radii of very low-mass NSs $\sim 1.1\,{\rm M}_\odot$ can be obtained through X-ray observations, or tidal deformability measurements of binary systems with very low chirp masses.

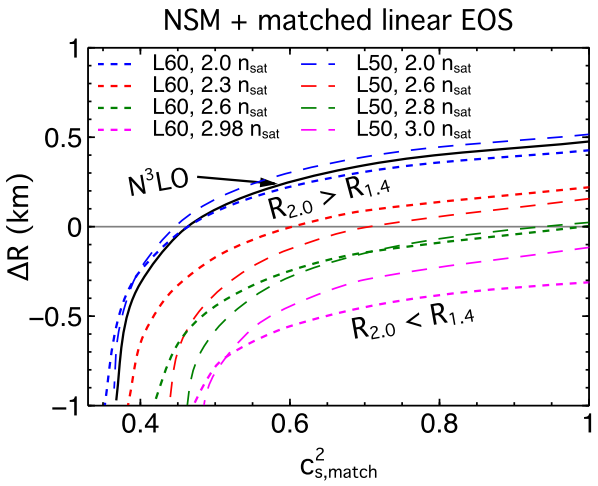

FIG. 14. Radius differences $\Delta R = R_{2.0} - R_{1.4}$ using the ZL extrapolations with $L = 50\,{\rm MeV}$ and $L = 60\,{\rm MeV}$ joined continuously to linear EOSs at $n_{\rm m}$ between $2.0\,n_{\rm sat}$ and $3.0\,n_{\rm sat}$.

From a different perspective, more accurate experimental determinations of S_v and L at $n_{\rm sat}$ from e.g., PREX, CREX, and FRIB/MSU, will be important to test χEFT predictions of properties of neutron-rich matter. At the present time, S_v and L are believed to be understood to the 10% and 40% levels, respectively [97]. For $n_{\rm B} > n_{\rm sat}$, constraints from the analyses of the collective flow of matter in HICs could be informative.

The best available information for the present comes from the analysis of HICs of Au nuclei using Boltzmann-type kinetic equations. The elliptic and sideways flow observables from these collisions are sensitive to the mean-

field potential and to in-medium NN collisions at central densities of $2-5\,n_{\rm sat}$, and suggest SNM pressures of $7.5\,{\rm MeV\,fm^{-3}}$ to $14\,{\rm MeV\,fm^{-3}}$ at $2.0\,n_{\rm sat}$ [117]. In comparison, N^{3}LO calculations for SNM predict somewhat larger pressures of $10.5\,{\rm MeV\,fm^{-3}}$ to $18.5\,{\rm MeV\,fm^{-3}}$ at $2.0\,n_{\rm sat}$ [42], which are, nevertheless, consistent within their stated 1σ uncertainties. However, the predictions from HICs involve model-dependent assumptions concerning the density- and momentum-dependencies of the assumed nuclear interactions, which have not been systematically explored; see Ref. [118] and references therein for the relevance of single-particle potentials in HICs. In addition to these uncertainties, HICs probe nearly symmetric matter, and to apply their observables to NSM requires an additional extrapolation involving the symmetry energy at supra-nuclear densities.

To improve the current status, heavy-ion facilities across the world, such as RHIC, FAIR, NICA, J-PARC, and HIAF, have launched programs to map out the QCD phase diagram of strongly interacting matter. The study of more neutron-rich matter in HICs, together with improved, systematic, modeling would be very valuable for dense-matter physics, not only for cold neutron stars, but also for understanding mergers involving NSs. As the analyses of HIC data have largely been done with nucleonic degrees of freedom, it would be also interesting and desirable to extend such analyses to include quark degrees of freedom and their subsequent hadronization as in RHIC and CERN experiments at higher energies.

B. $2.6\,{\rm M}_\odot$ neutron stars and the nature of the components of GW190425 and GW190814

The ranges of $1.6-2.5\,{\rm M}_\odot$ in GW190425 [119] and $2.59^{+0.08}_{-0.09}\,{\rm M}_\odot$ in GW190814 [120] for one of the components in these merger events have raised the possibility that those compact objects could be NSs as opposed to being low-mass BHs. The data from GW190425 was inconclusive concerning the nature of the inspiralling binary [119], but some works favored the scenario in which the more massive component is a BH instead of a very heavy NS [121]. If it is *a priori* assumed that $M_{\rm max}\lesssim 2.3\,{\rm M}_\odot$, a possibility motivated by EM and GW data from GW170817, the interpretation that it was a BNS merger instead statistically favors masses of approximately $1.5\pm0.2\,{\rm M}_\odot$ and $1.9\pm0.2\,{\rm M}_\odot$, while a neutron-star-black-hole (NSBH) merger interpretation favors a $1.3\pm0.1\,{\rm M}_\odot$ NS and a $2.2\pm0.2\,{\rm M}_\odot$ BH [121]. While both scenarios are statistically equally likely, the fact that the BNS masses are incompatible with those of observed galactic BNS systems, while the NS mass in the NSBH scenario is compatible, seems to favor the NSBH interpretation. However, in either scenario according to this analysis, GW190425 would likely not contain a NS $>2.1\,{\rm M}_\odot$. In the case of GW190814, there is no additional information, aside from one's assumption about $M_{\rm max}$, to decide if the primary is a high-mass NS or a low-mass BH. However, statistical analyses suggest that the probability of it's secondary being a NS is very low [47, 48, 120]. If either GW190425 or GW190814 contains a $\sim 2.5-2.6\,{\rm M}_\odot$ NS, questions to address are: *What is the physical state of dense matter that could support such a heavy NS, and what radius constraints would follow?*

The scenario that GW190814's secondary component was an approximately $2.6\,{\rm M}_\odot$ NS does not itself violate theoretical limits from causality and the GW170817 constraint that $\tilde\Lambda<720$ for $\mathcal{M}=1.186\,{\rm M}_\odot$, but challenges remain finding physical mechanisms that can connect very stiff high-density matter with the relatively soft nuclear matter at $\lesssim 2.0\,n_{\rm sat}$ predicted from modern χEFT calculations. As Fig. 6 shows, the conformal limit $c_s^2\le 1/3$ must be violated [111] below the central density of the maximum-mass star even by the requirements from pulsar timing that $M_{\rm max}\gtrsim 2.1\,{\rm M}_\odot$ and from GW170817's tidal deformability constraint. Standard extrapolations that assume gradually increasing c_s^2 profiles are unlikely to be compatible with $M_{\rm max}\ge 2.6\,{\rm M}_\odot$ [120].

In particular, the requirement that c_s^2 remains above ~ 0.6 for a wide range of densities $\gtrsim 2.0\,n_{\rm sat}$ is hard to explain. Extrapolations of non-relativistic potential models generally result in steadily increasing sound speeds with density, and it becomes problematic to prevent them from becoming acausal within NSs. At densities relevant to the center of very massive NSs, it is reasonable to expect the emergence of exotic degrees of freedom. A sharp first-order transition to stiff quark matter at some intermediate density is capable of reconciling small radii and high masses $\gtrsim 2.4\,{\rm M}_\odot$ (see examples of $R_{\rm min}(M)$ in Sec. IV C). With an increasing lower bound on $M_{\rm max}$ and/or smaller assumed values of c_s^2 at high densities, the transition threshold has to be pushed downward approaching $1.5-2.0\,n_{\rm sat}$ (similar to the results shown in Fig. 6 but involving a discontinuity $\Delta\varepsilon$ that further decreases $M_{\rm max}$ and favors lower values of $n_{\rm m}$ [89]).

For most microscopic quark-matter models, for example the original MIT bag model [122], the original Nambu-Jona–Lasinio (NJL) model [123], and their variations, perturbative QCD matter [124], and quartic polynomial parametrizations [125], the speed of sound turns out to be weakly density-dependent. To be consistent with massive pulsars $\sim 2\,{\rm M}_\odot$, strong repulsive interactions that stiffen the quark EOS, possibly reaching $c_s^2\ge 0.4$, have been implemented [126–128]. The maximally achievable c_s^2 is model-dependent, and requiring $c_s^2\gtrsim 0.6$ on average in quark matter is expected to push model parameters to extreme values.

In contrast to sharp phase transitions, hadron-to-quark crossovers as in quarkyonic models [79, 93, 129] or with interpolation schemes [130] provide a natural stiffening to support high masses, but can also induce large radii. Quarkyonic models generate large values of c_s^2 by restricting the nucleonic momentum phase space when quarks appear, and in some cases are capable of simultaneously reaching $>2.5\,{\rm M}_\odot$ and satisfying the GW170817 constraint $\tilde\Lambda_{1.186}<720$. Some versions [79], in which quarks

come to rapidly dominate the composition, leading to a high, but narrow, c_s^2 peak behavior, cannot jointly satisfy these conditions, reaching at most $M_{\rm max} \simeq 2.4\,{\rm M}_\odot$. However, we find that other versions [93, 129], in which the quark abundances grow more slowly and that can retain large abundances of nucleons at high density, can simultaneously achieve these conditions.

Using extrapolation functions in terms of c_s^2 and μ, Annala *et al.* [131] found that the risk of hadronic EOSs violating causality at high-enough densities ($\gtrsim 4.0\,n_{\rm sat}$) to achieve high masses is remedied if a transition to perturbative QCD-like (soft $c_s^2 \approx 1/3$) quark matter occurs at high densities. However, considering that current calculations in perturbative QCD itself are only valid at densities $n_{\rm B} \gtrsim 40\,n_{\rm sat}$, interpolations down to NS densities are problematic. The main feature of such a transition can be reproduced by simply requiring $c_s^2 \to 1/3$ for $n_{\rm B} \gtrsim 6\,n_{\rm sat}$, but at intermediate densities the conformal limit $c_s^2 \leq 1/3$ being violated is strongly favored [111]. Moreover, despite the fact that hadronic matter breaking the causal limit is never a necessity, it is nearly impossible to distinguish such high-density transitions using observations of the M–R relation or tidal deformabilities due to the masquerade problem [125].

C. Theoretical aspects of the dense matter EOS

In this study, we have used microscopic calculations of the EOS of PNM and SNM with χEFT NN and 3N interactions up to N^{3}LO to construct the EOS of NSM. N^{3}LO is currently the highest order in the χEFT expansion at which all two- and many-body interactions have been derived. This study was possible because recent advances in MBPT [35] have enabled significantly improved PNM predictions at this order, and, for the first time, provided order-by-order calculations of the SNM EOS with NN and 3N interactions up to N^{3}LO [35, 42, 44]. The underlying assumptions are that nucleons are the relevant degrees of freedom in this density range, and that χEFT provides a systematic expansion for the EOS to calculate EFT truncation errors. While these are reasonable assumptions, several questions remain and more work is needed to address them.

Experimental validation of χEFT predictions for the EOS of bulk matter relies on comparisons to the empirical saturation point, and constraints on the nuclear symmetry energy and its derivative with respect to density at $n_{\rm sat}$. While the MBPT calculations used in this work are well within the joint experimental constraint in the S_v–L plane [42], the $\Lambda = 500\,{\rm MeV}$ Hamiltonians—as discussed in Ref. [35]—actually do not saturate inside the empirical range for the saturation point, $n_{\rm sat} = 0.164 \pm 0.007\,{\rm fm}^{-3}$ with $(E/A)_{\rm sat} = -15.86 \pm 0.57\,{\rm MeV}$. Note, however, that this empirical range was obtained in Refs. [35, 67] from a set of energy density functionals, and thus only has limited statistical meaning. The predicted 2σ confidence ellipses for the nuclear saturation point at N^{2}LO and N^{3}LO are shown in Fig. 9 of Ref. [43].

Nuclear saturation in SNM emerges from a delicate cancellation of different contributions in the nuclear Hamiltonian, in contrast to the properties of neutron-rich NSM EOS. This cancellation is sensitive to the short- and intermediate-range 3N interactions at N^{2}LO that do not contribute to the PNM EOS; e.g., the 3N contact interaction ($\propto c_E$) is Pauli-blocked in PNM [63]. Together with the fact that the proton fraction is small, this means that the nuclear saturation properties are of relatively minor importance for constructing the NSM EOS. Nonetheless, a better understanding of nuclear saturation properties may help identify and quantify systematic uncertainties in the nuclear interactions. This might also lead to a better understanding of the link between (saturation) properties of infinite matter and medium-mass to heavy nuclei [132, 133] to explain why χEFT potentials generally tend to underestimate charge radii [134–136]. In this context, it is worth noting that systematic EFT calculations of the EOS of NSM, which is characterized by a small proton fraction, would obviate the need to rely on the quadratic expansion Eq. (20) (see, e.g., Ref. [31] in which the energy of adding a proton to PNM was calculated). When such calculations become available one can gauge the extent to which the EOS of NSM is correlated with the empirical properties of SNM.

Developing and applying improved order-by-order χEFT NN and 3N potentials up to N^{3}LO within different regularization schemes to finite nuclei and infinite matter is an important task for future work [132, 133, 136–138]. While this work has already accounted for correlated EFT truncation errors (as recently derived by the BUQEYE collaboration), uncertainties in the low-energy couplings at a given χEFT order, e.g., from fitting the nuclear interactions, have not been considered. Bayesian parameter estimation can be used to obtain low-energy couplings with statistically robust uncertainties [139–141]. A full Bayesian analysis of the EOS would then enable a consistent quantification and propagation of theoretical uncertainties, from those in the fits of the nuclear interactions to EFT truncation errors, via Monte Carlo sampling and the Jupyter notebooks provided by the BUQEYE collaboration [41].

Finally, we note that theoretical studies to access the EOS of matter at $n_{\rm B} \gtrsim 2\,n_{\rm sat}$ can have a significant impact on NS properties, especially on the correlation between $M_{\rm max}$ and the NS radii. Detailed studies of EFT truncation errors at these higher densities, especially in χEFT formulations with explicit Δ intermediate states would be valuable. Models that include additional degrees of freedom such as pions, hyperons, and quarks while still being able to accommodate massive NSs can provide new insights. Further work is needed to improve these models. Together with advances in nuclear-matter calculations from χEFT at low densities (see, e.g., Refs. [35, 36]), these will enable astrophysical applica-

tions based on microscopic calculations over a wide range in density and proton fraction.

D. Comparison with other works

As noted earlier, the uncertain nature of the less compact object in GW190814 with mass $\simeq 2.6\,\mathrm{M}_\odot$ has piqued the interest of the dense-matter and nuclear-physics communities. Below we briefly discuss how our study differs from or complements the findings of several other recent articles [45–52] that have addressed the implications of the possible existence of NSs with such high masses.

Several of these articles, including Refs. [45, 47, 49], have relied on nuclear physics based EOSs to describe matter in the crust and outer core to show that the existence of a 2.6 $\mathrm{M}_\odot$ NS would require $c_s^2 \geq 0.6$ in the inner core. The authors of Ref. [52] use the upper bound on the tidal deformability of NSs set by GW170817 to further strengthen the need for a large c_s^2 in the inner core. Most notably, Ref. [51] derives strict upper bounds on the maximum mass of NSs that depend only on bulk properties of NSs, such as the radii and the tidal deformabilities to find that a NS in GW190814 would not be inconsistent with present astronomical constraints if c_s^2 is large in the inner core. Our finding suggests that a 2.6 $\mathrm{M}_\odot$ NS would require $c_s^2 \geq 0.55 - 0.6$ (see Fig. 6 (a)) in the inner core, which is in general agreement with these earlier studies. A unique feature of our study is the use of the N^{3}LO-χEFT EOS that allows us to properly incorporate EFT truncation errors at $n_\mathrm{B} \leq 2.0\,n_\mathrm{sat}$.

Lim *et al.* [46] combine nuclear models valid in the vicinity of normal nuclear densities and a maximally stiff EOS at higher density to show that $2.5 - 2.6\,\mathrm{M}_\odot$ NS can exist without strongly affecting the properties such as radius, tidal deformability, and moment of inertia of canonical NSs with mass $\sim 1.4\,\mathrm{M}_\odot$. They argue that properties of NSs with masses $\sim 2\,\mathrm{M}_\odot$ such as $R_{\sim 2.14}$ would be significantly different depending on whether the secondary component of GW190814 was a black hole or a NS. Our results support these findings, but go beyond by delineating how the lower and upper bounds on the radii of NSs in the mass range $1.4 - 2\,\mathrm{M}_\odot$ would be constrained if future observations were to confirm the existence of NSs with masses $\simeq 2.5 - 2.6\,\mathrm{M}_\odot$.

Using FSU-type relativistic mean field-theoretical (RMFT) models, Fattoyev *et al.* [50] found that the rapid increase in pressure with density required to support a 2.6 $\mathrm{M}_\odot$ NS, while barely accommodating the deformability constraint from the first analysis of GW170817 data that indicates $\Lambda_{1.4} \leq 800$ [5] but not the updated bounds $70 \leq \Lambda_{1.4} \leq 580$ [7] (see Ref. [142] for a similar study), is inconsistent with energy density functionals tuned to reproduce properties of nuclei and flow data from HICs. Note that Fattoyev *et al.* [50] only applied $\Lambda_{1.4}$ constraint without a comparison of the binary tidal deformability $\tilde{\Lambda}$. We have confirmed that FSU-like RMFT interactions cannot accommodate both $\tilde{\Lambda}_{1.186} \leq 720$ and $M_\mathrm{max} \geq 2.54\,\mathrm{M}_\odot$ [115].

Other recent works studied hyperonic matter in the EOS and/or rapid rotations that stabilize more massive stars than non-rotating configurations, which may or may not be consistent with GW190814 [143–146]; we do not consider these effects in the present paper.

VI. CONCLUSIONS

In this paper, we have highlighted the important role M_max plays in determining bounds on the radii of neutron stars. In the most extreme case, in which only causality is assumed with the EOS $\varepsilon = \varepsilon_0 + P$, absolute upper bounds on $M_\mathrm{max} \simeq 4.09\,\mathrm{M}_\odot$ and $R_{M_\mathrm{max}} \simeq 17.1\,\mathrm{km}$ exist as long as $\varepsilon_0 > \varepsilon_\mathrm{sat}$ (Eq. (4) and Eq. (5)). Firm lower bounds on $R_\mathrm{min}(M)$ and R_{M_max} that scale with M_max can also be established. For the case that $M_\mathrm{max} = 2.0\,\mathrm{M}_\odot$, $R_\mathrm{min}(1.4\,\mathrm{M}_\odot) = 8.2$ km and $R_{M_\mathrm{max}} = 8.4$ km. Assuming that $M_\mathrm{max} \geq 2.6\,\mathrm{M}_\odot$, we find $R_\mathrm{min}(1.4\,\mathrm{M}_\odot) > 9.75\,\mathrm{km}$ and $R_\mathrm{min}(2.0\,\mathrm{M}_\odot) > 10.8\,\mathrm{km}$ (Table I).

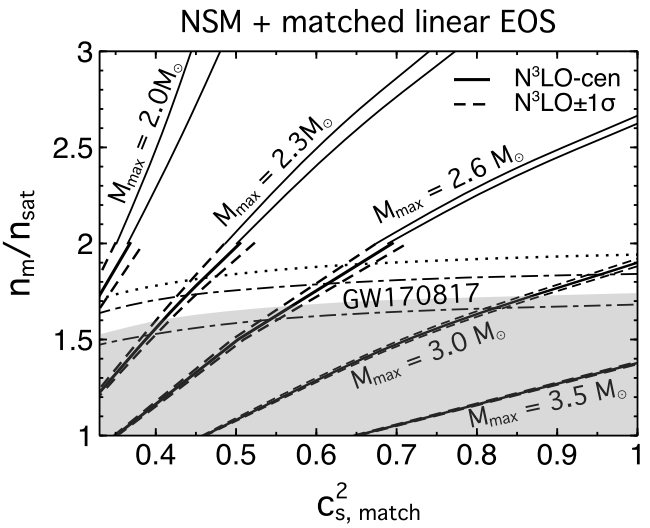

FIG. 15. The same plot as Fig. 6 but showing M_max contours on the $(c^2_{s,\mathrm{match}}, n_\mathrm{m})$ plane. Note that the GW170817 boundaries excluding $n_\mathrm{m} \lesssim 1.5 - 1.8\,n_\mathrm{sat}$ will be shifted downwards if there is first-order transition at such low densities.

If instead an upper limit $c_s^2 < 1$ is assumed so that $\varepsilon = \varepsilon_0 + P/c_s^2$, then $R_\mathrm{min}(M)$ and M_max depend sensitively on c_s^2 and decrease with it. For the case $c_s^2 = 1/3$ and $\varepsilon_0 = \varepsilon_\mathrm{sat}$, for example, $M_\mathrm{max} = 2.48\,\mathrm{M}_\odot$, $R_\mathrm{min}(1.4\,\mathrm{M}_\odot) = 12.8\,\mathrm{km}$, and $R_{M_\mathrm{max}} = 13.3\,\mathrm{km}$ (Fig. 1).

We determined the NSM EOS in beta-equilibrium from MBPT calculations of PNM and SNM up to N^{3}LO in χEFT. For a given n_B, the NSM EOS always has a lower

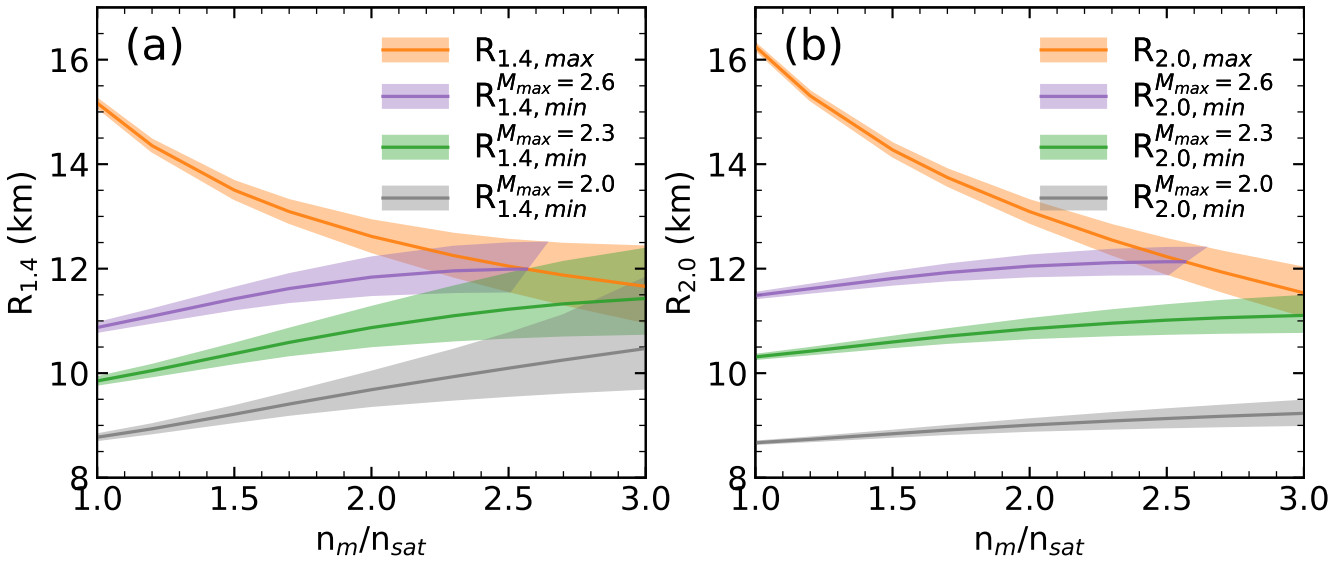

FIG. 16. Similar to Figs. 9 and 10, but displaying the minimum and maximum radii of $1.4\,\mathrm{M}_\odot$ (panel (a)) and $2.0\,\mathrm{M}_\odot$ (panel (b)) stars as a function of the matching density $n_\mathrm{m} = 1.0 - 3.0\,n_\mathrm{sat}$. Additionally, R_min contours and uncertainty bands for the case $M_\mathrm{max} = 2.3\,\mathrm{M}_\odot$ are shown.

ε than the PNM EOS. The pressure of NSM is less than PNM at the same n_B, typically by $< 1\,\mathrm{MeV\,fm^{-3}}$, except for $n_\mathrm{B} \gtrsim 2.0\,n_\mathrm{sat}$ when it becomes greater (Fig. 2 (b)). The proton fraction below $2.0\,n_\mathrm{sat}$ never exceeds the critical minimum value required for the direct URCA process of enhanced neutrino emission [147, 148].

The existence of the NS crust together with a nucleonic EOS below a matching density n_m establishes $R_\mathrm{max}(M)$. Extremes are again found by assuming $c^2_{s,\mathrm{match}} = 1$ for densities above n_m, for which the EOS is now $\varepsilon = \varepsilon_\mathrm{m} + P - P_\mathrm{m}$. Assuming $\varepsilon_\mathrm{m} = \varepsilon_\mathrm{sat}$, and that P_m is given by χEFT-N^{3}LO, the upper bounds are $R_{1.4,\mathrm{max}} \approx 15.1\,\mathrm{km}$ and $R_{2.0,\mathrm{max}} \approx 16.2\,\mathrm{km}$ (see Fig. 16 where $n_\mathrm{m} = n_\mathrm{sat}$), which are nearly identical to the case shown in Fig. 1 with a slightly different value of P_m at $\varepsilon_\mathrm{m} = \varepsilon_\mathrm{sat}$. These values are not in tension with observations, and with increasing n_m, the corresponding upper bounds on $R_{1.4}$ and $R_{2.0}$ decrease. For the same ε_m or n_m, M_max is not sensitive to the value of P_m or the nucleonic EOS between the crust and n_m, and is close to that of the case $P_0 = 0$ (self-bound stars) for the causal EOS; see also Fig. 3.

Using the N^{3}LO EOS between the crust and n_m, we determined how M_max depends on n_m and $c^2_{s,\mathrm{match}}$ (Fig. 15); we find that $M_\mathrm{max} \geq 2.6\,\mathrm{M}_\odot$ requires $c^2_{s,\mathrm{match}} > 0.35$ (i.e., the EOS violates the conformal limit $c_s^2 \leq 1/3$) if $n_\mathrm{m} = n_\mathrm{sat}$, and $c^2_{s,\mathrm{match}} > 0.7$ if $n_\mathrm{m} = 2.0\,n_\mathrm{sat}$. The conformal limit is also violated for $n_\mathrm{m} > 1.7\,n_\mathrm{sat}$, even if M_max is as low as $2.0\,\mathrm{M}_\odot$. If $M_\mathrm{max} > 2.45\,\mathrm{M}_\odot$, n_m must not exceed $3.0\,n_\mathrm{sat}$ no matter what the value of $c^2_{s,\mathrm{match}}$ is. The calibrated uncertainties in χEFT-N^{3}LO lead to relatively small uncertainties, less than $0.1\,\mathrm{M}_\odot$, in $M_\mathrm{max}(n_\mathrm{m}, c^2_{s,\mathrm{match}})$.

Additionally, satisfying the GW170817 tidal deformability constraint $\tilde{\Lambda}_{1.186} < 720$ and imposing $M_\mathrm{max} > 2.1\,\mathrm{M}_\odot$ requires $n_\mathrm{m} > 1.5\,n_\mathrm{sat}$ and $c_s^2 > 0.35$. This limit is not very sensitive to M_max. Even if $M_\mathrm{max} > 2.6\,\mathrm{M}_\odot$, it is required that $1.7 < n_\mathrm{m}/n_\mathrm{sat} < 2.6$ and $c^2_{s,\mathrm{match}} > 0.55$. The existence of a $2.6\,\mathrm{M}_\odot$ star evidently requires a significant change from normal hadronic EOSs to a much stiffer EOS between $1.7\,n_\mathrm{sat}$ and $2.6\,n_\mathrm{sat}$. In the presence of a discontinuity in ε, the lower bound $n_\mathrm{m} \gtrsim 1.7\,n_\mathrm{sat}$ can decrease, whereas the upper bound $n_\mathrm{m} \lesssim 2.6\,n_\mathrm{sat}$ remains unaffected as it is imposed by causality.

For stars with a normal crust, refined upper limits to R_{M_max} can be found using the GW10817 constraint and an assumed value for M_max, while lower limits follow from the causal EOS: 9 km $< R_{M_\mathrm{max}} <$ 12.2 km for $M_\mathrm{max} \leq 2.1\,\mathrm{M}_\odot$ and 11.3 km $< R_{M_\mathrm{max}} <$ 12.8 km for $M_\mathrm{max} \leq 2.6\,\mathrm{M}_\odot$.

The minimum radii $R_\mathrm{min}(M)$ established for the self-bound configurations are relaxed in the case of stars with normal nuclear-matter crusts, by using N^{3}LO up to n_m and applying a phase transition into the causal EOS ($c^2_{s,\mathrm{match}} = 1$) involving a finite discontinuity $\Delta\varepsilon_\mathrm{m}$ at n_m. These minimum radius bounds will be highly sensitive to the assumed M_max and steadily increase with it; see, e.g., Fig. 9. For the same value of n_m, the corresponding maximum radii $R_\mathrm{max}(M)$ follow by attaching to the causal EOS but without a density discontinuity, which gives rise to a unique value of M_max at a given n_m and therefore the maximum radius bounds do not rely on the assumptions about M_max.

The results shown in Figs. 9 and 10 are summarized in Fig. 16 for the specific cases of $R_{1.4}$ and $R_{2.0}$, with a broader range of n_m explored between $1.0 - 3.0\,n_\mathrm{sat}$. If

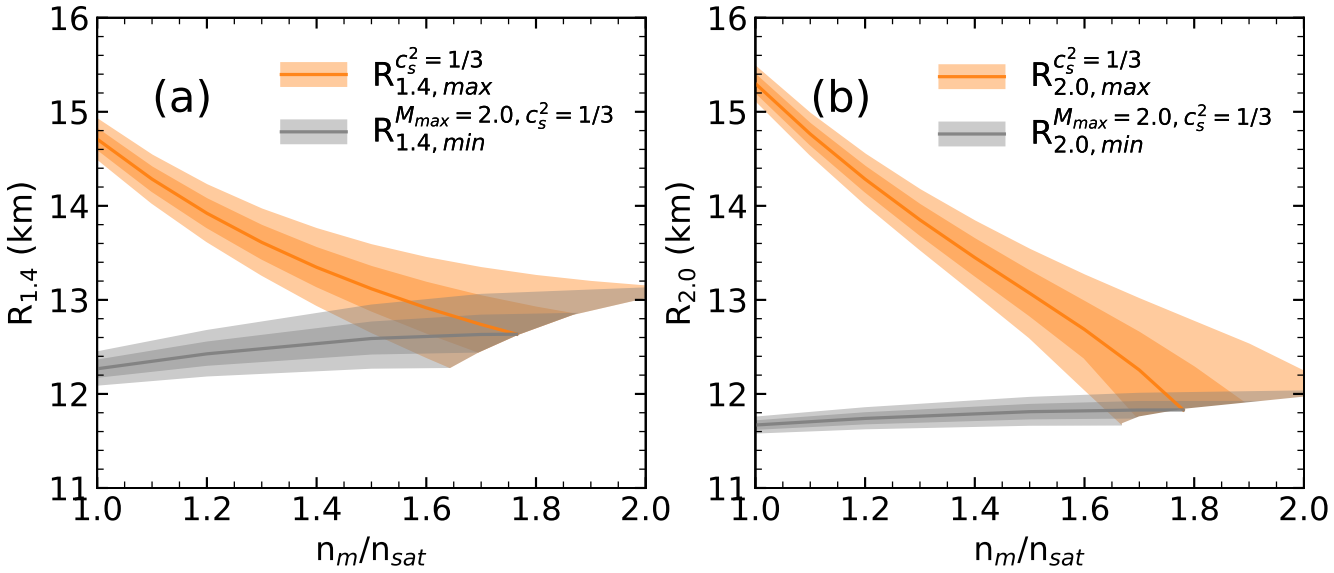

FIG. 17. The maximum (orange) and minimum (black) bounds on $R_{1.4}$ and $R_{2.0}$ assuming $c_s^2 \leq 1/3$ above $n_{\rm B} = n_{\rm m}$; χEFT-N^{3}LO uncertainties are indicated (darker bands: $\pm 1\sigma$; lighter bands: $\pm 2\sigma$). The bands merge and terminate at critical matching densities above which $M_{\rm max} < 2.0\,{\rm M}_\odot$.

χEFT-N^{3}LO is assumed valid up to $2.0\,n_{\rm sat}$, the upper and lower bounds on NS radii are substantially tightened in comparison with using χEFT-N^{3}LO only up to $n_{\rm sat}$: for example if $M_{\rm max} \geq 2.0\,{\rm M}_\odot$ then $R_{1.4}$ must lie between $12.5^{+0.3}_{-0.2}$ km and $9.7^{+0.4}_{-0.3}$ km at the 1σ level, which is consistent with earlier studies in Ref. [80].

Figure 16 also conveniently illustrates the dramatic effect of increasing the lower bound on $M_{\rm max}$ for the allowed ranges between $R_{\rm min}(M)$ and $R_{\rm max}(M)$, which improves (shrinks) the $R_{1.4}\,(R_{2.0})$ bounds by an average $3\,{\rm km/M}_\odot$ ($5\,{\rm km/M}_\odot$); these limits could be further restricted by forthcoming observations. We note that $R_{1.4}$ or $R_{2.0} < 10.7\,{\rm km}$ would be incompatible with $M_{\rm max} > 2.3\,{\rm M}_\odot$ (assuming $n_{\rm m} = 2.0\,n_{\rm sat}$). In addition, if future measurements from different sources and messengers, e.g., X-ray data from QLMXBs or PREs (or GW detections of mergers by LIGO) vs NICER targets, were to exhibit discrepancies in the radius inference close to or larger than the gaps between the minimum and maximum bands shown on this figure, then these are hints of a large energy-density discontinuity $\Delta\varepsilon$ in the EOS (accompanied with high-density stiff matter) occurring at $n_{\rm B} \lesssim n_{\rm m}$ [89].

There has been speculation that the speed of sound in QCD at finite baryon density may be bounded by the conformal limit which requires $c_s^2 < 1/3$ [149]. This speculation is in part based on strong-coupling calculations of SU(N_c) gauge theories for which a holographic or gravity dual exist. In these theories the speed of sound can be calculated at finite baryon density in the large-N_c limit using classical supergravity methods in a curved spacetime [150], and for a large class of such theories (for exceptions, see Refs. [151, 152]) $c_s^2 < 1/3$ [149, 153]. In addition, at finite temperature and zero baryon density, where lattice QCD calculations provide reliable predictions, $c_s^2 < 1/3$ at all temperatures. The sound speed increases rapidly in the hadronic phase (dominated by pions) reaching a maximum value $c_s^2 \simeq 0.2$, then decreases across hadron-quark cross-over region, corresponding to temperatures in the range $100 - 200\,{\rm MeV}$, and eventually increases again to reach its asymptotic value of $c_s^2 \simeq 1/3$ at $T \simeq 500\,{\rm MeV}$ [154].

Motivated by the discussion above, we briefly comment on the astrophysical implications of the conjecture that $c_s^2 < 1/3$ in QCD [149] in light of our results. It was already noted in Refs. [155, 156] that it is difficult to accommodate $c_s^2 < 1/3$ at high density and $M_{\rm max} > 2.0\,{\rm M}_\odot$ while still allowing for a soft EOS at intermediate density needed to ensure that $R_{1.4} < 13\,{\rm km}$. This is also evident from Fig. 15 which shows that when $c_s^2 < 1/3$, it is impossible, at the 1σ level, to simultaneously satisfy the tidal deformability constraint from GW170817 and $M_{\rm max} > 2.0\,{\rm M}_\odot$ if χEFT-N^{3}LO is valid beyond $1.8\,n_{\rm sat}$.

Figure 17 shows how the bounds on the radius are influenced when $c_s^2 < 1/3$ at high density. The rapid decrease in the maximum value of $R_{1.4}$ with $n_{\rm m}$ is striking and implies that if $c_s^2 < 1/3$ and χEFT-N^{3}LO is valid up to $1.5\,n_{\rm sat}$, then $R_{1.4}$ must lie between $12.4^{+0.2}_{-0.2}\,{\rm km}$ and $13.1^{+0.3}_{-0.3}\,{\rm km}$ at the 1σ level. Further, requiring that $M_{\rm max} > 2.0\,{\rm M}_\odot$ excludes a significant fraction of the χEFT-N^{3}LO predicted range for the pressure for densities between $1.5 - 2.0\,n_{\rm sat}$. A tiny sliver of high pressure close to the edge of the 2σ boundary remains, and im-

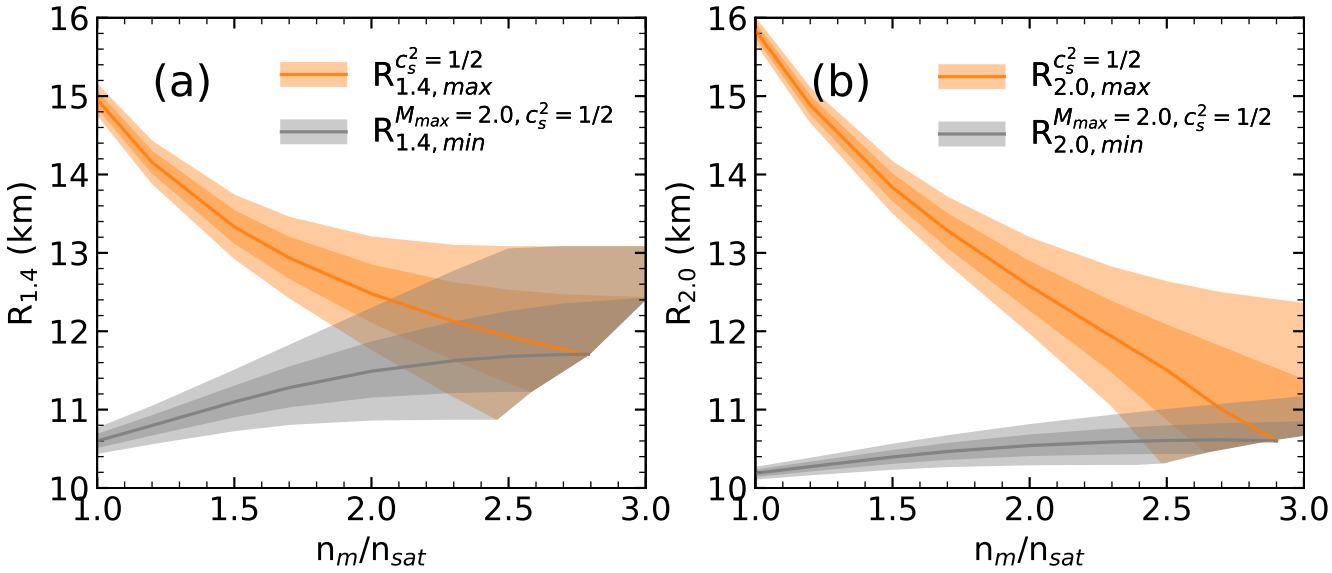

FIG. 18. Similar to Fig. 17, but assuming $c_s^2 \leq 1/2$ above $n_{\rm B} = n_{\rm m}$.

plies that $R_{1.4} = 13.1 \pm 0.1\,$km! Predictions for $R_{2.0}$ are shown in the right panel.

In Fig. 18 we show the maximum and minimum bounds on $R_{1.4}$ and $R_{2.0}$ obtained by imposing an intermediate limit of $c_s^2 \leq 1/2$. In this case for $n_{\rm m} = 2.0\,n_{\rm sat}$, we find that $11.5^{+0.3}_{-0.3}\,{\rm km} < R_{1.4} < 12.5^{+0.3}_{-0.2}\,{\rm km}$ and $M_{\rm max} < 2.29 \pm 0.04\ {\rm M}_\odot$ (Fig. 6 (b)), to 1σ confidence. The corollary to this implies that measurements of $R_{\sim 1.4}$ that are smaller than 11.2 km would favor a stiff EOS with $c_s^2 \geq 1/2$ above $2.0\,n_{\rm sat}$, or that $n_{\rm m} < 2.0\,n_{\rm sat}$. This is particularly interesting because a recent analysis of the tidal deformability constraints from GW170817 in Ref. [78] suggests $11.0^{+0.9}_{-0.6}\,$km (90% credible interval).

We also quantified the sensitivity of the key observables $R_{1.4}$, $R_{2.0}$, and $M_{\rm max}$ to the pressure as a function of density $P(n_{\rm B})$, and found that the highest correlations, i.e., the most sensitive regions, involve the density ranges $1.0-3.0\,n_{\rm sat}$, $1.5-4.0\,n_{\rm sat}$, and $2.0-6.0\,n_{\rm sat}$, respectively.

We showed that positive values of $\Delta R = R_{2.0} - R_{1.4}$, potentially possible with NICER, would indicate low matching densities $\lesssim 2.0 - 2.5\,n_{\rm sat}$ and relatively large values of $c^2_{s,{\rm match}} \gtrsim 0.45 - 0.6$, which would also imply large values of $M_{\rm max}$. In the absence of a dramatic stiffening of the EOS near $2.0\,n_{\rm sat}$, the expectation is that $\Delta R < 0$. This is usually the case if extrapolations based on nucleonic-like models are used up to even higher densities and/or there is extra softening below $M_{\rm max}$.

The merger events GW190425 and GW190814 are each consistent with at least one component $\gtrsim 2.5\,{\rm M}_\odot$ which could be either a massive NS or a low-mass BH, although GW190425 could instead involve two $\sim 1.7\,{\rm M}_\odot$ NSs. Should either system contain a NS with $M \gtrsim 2.5\,{\rm M}_\odot$, the implications would be that the conformal limit $c_s^2 \leq 1/3$ is almost certainly violated (since $n_{\rm m}$ is likely larger than $n_{\rm sat}$); if $n_{\rm m} > 1.5\,n_{\rm sat}$ $(2.0\,n_{\rm sat})$, the average c_s^2 above $n_{\rm m}$ should be > 0.5 (0.67). More importantly, in order to also satisfy the small binary tidal deformability inferred from GW170817, $n_{\rm m} \gtrsim 1.65\,n_{\rm sat}$ (could be lowered if there is sudden softening in the EOS induced by a strong first-order transition) and $c^2_{s,{\rm match}} \gtrsim 0.6$ are necessary. These conditions are typically not satisfied by most microscopic quark models unless parametrizations with explicit large sound speeds, or some crossover-like transitions that can be realized in, e.g., quarkyonic matter, are assumed. Even in the crossover scenario, severe constraints would follow and require fine-tuning of model parameters.

Our studies have highlighted the interplay of $M_{\rm max}$, the radii of NSs, and the role of the nucleonic EOS for densities beyond $n_{\rm sat}$. We have illustrated that χEFT calculations provide an EOS for NSM up to $\sim 2.0\,n_{\rm sat}$ with quantifiable EFT uncertainties [42, 43], and moreover, these uncertainties are small enough to have relatively minor influence on our major conclusions. Nevertheless, our results reveal that a reliable extension of the EOS to densities moderately in excess of $2.0\,n_{\rm sat}$ is greatly desired, and could provide important additional constraints on the relations among $M_{\rm max}$, $R_{\rm min}(M)$, and $R_{\rm max}(M)$. These theoretical relationships would be soon confronted with X-ray, radio, and GW observations.

ACKNOWLEDGMENTS

We thank R. J. Furnstahl, B.-A. Li, J. A. Melendez, and D. R. Phillips for useful discussions, and the Network for Neutrinos, Nuclear Astrophysics, and Symmetries (N3AS) for encouragement and support. C.D. ac-

knowledges support by the Alexander von Humboldt Foundation through a Feodor-Lynen Fellowship and the U.S. Department of Energy, the Office of Science, the Office of Nuclear Physics, and SciDAC under awards DE-SC00046548 and DE-AC02-05CH11231. S.H. is supported by the National Science Foundation, Grant PHY-1630782, and the Heising-Simons Foundation, Grant 2017-228. J.M.L. and T.Z. acknowledge support by the U.S. DOE under Grant No. DE-FG02-87ER40317 and by NASA's NICER mission with Grant 80NSSC17K0554. M.P.'s research was supported by the Department of Energy, Grant No. DE-FG02-93ER40756. The work of S.R. was supported by the U.S. DOE under Grant No. DE-FG02-00ER41132.

[1] S. Gandolfi, J. Carlson, and S. Reddy, Phys. Rev. C **85**, 032801 (2012), arXiv:1101.1921 [nucl-th].
[2] J. Lattimer and M. Prakash, Astrophys. J. **550**, 426 (2001), arXiv:astro-ph/0002232.
[3] B. Margalit and B. D. Metzger, Astrophys. J. Lett. **850**, L19 (2017), arXiv:1710.05938 [astro-ph.HE].
[4] M. Shibata, E. Zhou, K. Kiuchi, and S. Fujibayashi, Phys. Rev. D **100**, 023015 (2019), arXiv:1905.03656 [astro-ph.HE].
[5] B. Abbott *et al.* (LIGO Scientific, Virgo), Phys. Rev. Lett. **119**, 161101 (2017), arXiv:1710.05832 [gr-qc].
[6] B. Abbott *et al.* (LIGO Scientific, Virgo), Phys. Rev. X **9**, 011001 (2019), arXiv:1805.11579 [gr-qc].
[7] B. Abbott *et al.* (LIGO Scientific, Virgo), Phys. Rev. Lett. **121**, 161101 (2018), arXiv:1805.11581 [gr-qc].
[8] P. Demorest, T. Pennucci, S. Ransom, M. Roberts, and J. Hessels, Nature **467**, 1081 (2010), arXiv:1010.5788 [astro-ph.HE].
[9] J. Antoniadis *et al.*, Science **340**, 6131 (2013), arXiv:1304.6875 [astro-ph.HE].
[10] E. Fonseca *et al.*, Astrophys. J. **832**, 167 (2016), arXiv:1603.00545 [astro-ph.HE].
[11] Z. Arzoumanian *et al.* (NANOGrav), Astrophys. J. Suppl. **235**, 37 (2018), arXiv:1801.01837 [astro-ph.HE].
[12] H. T. Cromartie *et al.*, Nature Astron. **4**, 72 (2019), arXiv:1904.06759 [astro-ph.HE].
[13] F. Özel and P. Freire, Ann. Rev. Astron. Astrophys. **54**, 401 (2016), arXiv:1603.02698 [astro-ph.HE].
[14] G. B. Rybicki, C. O. Heinke, R. Narayan, and J. E. Grindlay, Astrophys. J. **644**, 1090 (2006), arXiv:astro-ph/0506563.
[15] F. Özel, T. Guver, and D. Psaltis, Astrophys. J. **693**, 1775 (2009), arXiv:0810.1521 [astro-ph].
[16] S. Bogdanov, G. B. Rybicki, and J. E. Grindlay, Astrophys. J. **670**, 668 (2007), arXiv:astro-ph/0612791.
[17] M. C. Miller, Astrophys. J. **822**, 27 (2016), arXiv:1602.00312 [astro-ph.HE].
[18] A. Watts *et al.*, PoS **AASKA14**, 043 (2015), arXiv:1501.00042 [astro-ph.SR].
[19] E. Epelbaum, H.-W. Hammer, and U.-G. Meissner, Rev. Mod. Phys. **81**, 1773 (2009), arXiv:0811.1338 [nucl-th].
[20] R. Machleidt and D. Entem, Phys. Rept. **503**, 1 (2011), arXiv:1105.2919 [nucl-th].
[21] H.-W. Hammer, S. Knig, and U. van Kolck, Rev. Mod. Phys. **92**, 025004 (2020), arXiv:1906.12122 [nucl-th].
[22] I. Tews, Z. Davoudi, A. Ekstrm, J. D. Holt, and J. E. Lynn, J. Phys. G **47**, 103001 (2020), arXiv:2001.03334 [nucl-th].
[23] I. Tews, T. Krger, K. Hebeler, and A. Schwenk, Phys. Rev. Lett. **110**, 032504 (2013), arXiv:1206.0025 [nucl-th].
[24] K. Hebeler, J. Lattimer, C. Pethick, and A. Schwenk, Astrophys. J. **773**, 11 (2013), arXiv:1303.4662 [astro-ph.SR].
[25] G. Baardsen, A. Ekstrm, G. Hagen, and M. Hjorth-Jensen, Phys. Rev. C **88**, 054312 (2013), arXiv:1306.5681 [nucl-th].
[26] C. Drischler, V. Soma, and A. Schwenk, Phys. Rev. C **89**, 025806 (2014), arXiv:1310.5627 [nucl-th].
[27] G. Hagen, T. Papenbrock, A. Ekstrm, K. Wendt, G. Baardsen, S. Gandolfi, M. Hjorth-Jensen, and C. Horowitz, Phys. Rev. C **89**, 014319 (2014), arXiv:1311.2925 [nucl-th].
[28] A. Carbone, A. Rios, and A. Polls, Phys. Rev. C **88**, 044302 (2013), arXiv:1307.1889 [nucl-th].
[29] L. Coraggio, J. Holt, N. Itaco, R. Machleidt, L. Marcucci, and F. Sammarruca, Phys. Rev. C **89**, 044321 (2014), arXiv:1402.0965 [nucl-th].
[30] C. Wellenhofer, J. W. Holt, N. Kaiser, and W. Weise, Phys. Rev. C **89**, 064009 (2014), arXiv:1404.2136 [nucl-th].
[31] A. Roggero, A. Mukherjee, and F. Pederiva, Phys. Rev. Lett. **112**, 221103 (2014), arXiv:1402.1576 [nucl-th].
[32] J. Holt and N. Kaiser, Phys. Rev. C **95**, 034326 (2017), arXiv:1612.04309 [nucl-th].
[33] C. Drischler, A. Carbone, K. Hebeler, and A. Schwenk, Phys. Rev. C **94**, 054307 (2016), arXiv:1608.05615 [nucl-th].
[34] A. Ekstrm, G. Hagen, T. Morris, T. Papenbrock, and P. Schwartz, Phys. Rev. C **97**, 024332 (2018), arXiv:1707.09028 [nucl-th].
[35] C. Drischler, K. Hebeler, and A. Schwenk, Phys. Rev. Lett. **122**, 042501 (2019), arXiv:1710.08220 [nucl-th].
[36] D. Lonardoni, I. Tews, S. Gandolfi, and J. Carlson, Phys. Rev. Res. **2**, 022033 (2020), arXiv:1912.09411 [nucl-th].
[37] M. Piarulli, I. Bombaci, D. Logoteta, A. Lovato, and R. Wiringa, Phys. Rev. C **101**, 045801 (2020), arXiv:1908.04426 [nucl-th].
[38] K. Hebeler, J. Holt, J. Menendez, and A. Schwenk, Ann. Rev. Nucl. Part. Sci. **65**, 457 (2015), arXiv:1508.06893 [nucl-th].
[39] C. Drischler, W. Haxton, K. McElvain, E. Mereghetti, A. Nicholson, P. Vranas, and A. Walker-Loud (2019) arXiv:1910.07961 [nucl-th].
[40] F. Sammarruca and R. Millerson, Front. in Phys. **7**, 213 (2019).
[41] BUQEYE collaboration (2020) `https://buqeye.github.io/software/`.
[42] C. Drischler, R. Furnstahl, J. Melendez, and D. Phillips (2020) arXiv:2004.07232 [nucl-th].

[43] C. Drischler, J. Melendez, R. Furnstahl, and D. Phillips (2020) arXiv:2004.07805 [nucl-th].
[44] M. Leonhardt, M. Pospiech, B. Schallmo, J. Braun, C. Drischler, K. Hebeler, and A. Schwenk (2019) arXiv:1907.05814 [nucl-th].
[45] H. Tan, J. Noronha-Hostler, and N. Yunes (2020) arXiv:2006.16296 [astro-ph.HE].
[46] Y. Lim, A. Bhattacharya, J. W. Holt, and D. Pati (2020) arXiv:2007.06526 [nucl-th].
[47] I. Tews, P. T. Pang, T. Dietrich, M. W. Coughlin, S. Antier, M. Bulla, J. Heinzel, and L. Issa (2020) arXiv:2007.06057 [astro-ph.HE].
[48] R. Essick and P. Landry (2020) arXiv:2007.01372 [astro-ph.HE].
[49] A. Tsokaros, M. Ruiz, and S. L. Shapiro (2020) arXiv:2007.05526 [astro-ph.HE].
[50] F. Fattoyev, C. Horowitz, J. Piekarewicz, and B. Reed (2020) arXiv:2007.03799 [nucl-th].
[51] D. A. Godzieba, D. Radice, and S. Bernuzzi (2020) arXiv:2007.10999 [astro-ph.HE].
[52] A. Kanakis-Pegios, P. Koliogiannis, and C. Moustakidis (2020) arXiv:2007.13399 [nucl-th].
[53] S. Koranda, N. Stergioulas, and J. L. Friedman, Astrophys. J. **488**, 799 (1997), arXiv:astro-ph/9608179.
[54] R. C. Tolman, Phys. Rev. **55**, 364 (1939).
[55] J. Oppenheimer and G. Volkoff, Phys. Rev. **55**, 374 (1939).
[56] J. M. Lattimer, M. Prakash, D. Masak, and A. Yahil, Astrophys. J. **355**, 241 (1990).
[57] J. W. Negele and D. Vautherin, Nucl. Phys. A **207**, 298 (1973).
[58] G. Baym, C. Pethick, and P. Sutherland, Astrophys. J. **170**, 299 (1971).
[59] J. Melendez, S. Wesolowski, and R. Furnstahl, Phys. Rev. C **96**, 024003 (2017), arXiv:1704.03308 [nucl-th].
[60] J. Melendez, R. Furnstahl, D. Phillips, M. Pratola, and S. Wesolowski, Phys. Rev. C **100**, 044001 (2019), arXiv:1904.10581 [nucl-th].
[61] T. Krger, I. Tews, K. Hebeler, and A. Schwenk, Phys. Rev. C **88**, 025802 (2013), arXiv:1304.2212 [nucl-th].
[62] D. Entem, R. Machleidt, and Y. Nosyk, Phys. Rev. C **96**, 024004 (2017), arXiv:1703.05454 [nucl-th].
[63] K. Hebeler and A. Schwenk, Phys. Rev. C **82**, 014314 (2010), arXiv:0911.0483 [nucl-th].
[64] P. Bevington and D. Robinson, *Data Reduction and Error Analysis for the Physical Sciences*, 3rd ed. (McGraw-Hill, 2003).
[65] J. D. Evans, *Straightforward Statistics for the Behavioral Sciences* (Brooks/Cole Publishing, Pacific Grove, Calif., 1996).
[66] A. G. Asuero, A. Sayago, and A. G. González, Crit. Rev. Anal. Chem. **36**, 41 (2006).
[67] C. Drischler, K. Hebeler, and A. Schwenk, Phys. Rev. C **93**, 054314 (2016), arXiv:1510.06728 [nucl-th].
[68] N. Kaiser, Phys. Rev. C **91**, 065201 (2015), arXiv:1504.00604 [nucl-th].
[69] C. Wellenhofer, J. W. Holt, and N. Kaiser, Phys. Rev. C **93**, 055802 (2016), arXiv:1603.02935 [nucl-th].
[70] R. Somasundaram, C. Drischler, I. Tews, and J. Margueron (2020) arXiv:2009.04737.
[71] T. Damour and A. Nagar, Phys. Rev. D **80**, 084035 (2009), arXiv:0906.0096 [gr-qc].
[72] T. Hinderer, B. D. Lackey, R. N. Lang, and J. S. Read, Phys. Rev. D **81**, 123016 (2010), arXiv:0911.3535 [astro-ph.HE].
[73] S. Postnikov, M. Prakash, and J. M. Lattimer, Phys. Rev. D **82**, 024016 (2010), arXiv:1004.5098 [astro-ph.SR].
[74] T. Dietrich *et al.*, Phys. Rev. D **99**, 024029 (2019), arXiv:1804.02235 [gr-qc].
[75] T. Zhao and J. M. Lattimer, Phys. Rev. D **98**, 063020 (2018), arXiv:1808.02858 [astro-ph.HE].
[76] S. De, D. Finstad, J. M. Lattimer, D. A. Brown, E. Berger, and C. M. Biwer, Phys. Rev. Lett. **121**, 091102 (2018), [Erratum: Phys.Rev.Lett. 121, 259902 (2018)], arXiv:1804.08583 [astro-ph.HE].
[77] P. Landry and R. Essick, Phys. Rev. D **99**, 084049 (2019), arXiv:1811.12529 [gr-qc].
[78] C. D. Capano, I. Tews, S. M. Brown, B. Margalit, S. De, S. Kumar, D. A. Brown, B. Krishnan, and S. Reddy, Nature Astron. **4**, 625 (2020), arXiv:1908.10352 [astro-ph.HE].
[79] T. Zhao and J. M. Lattimer, Phys. Rev. D **102**, 023021 (2020), arXiv:2004.08293 [astro-ph.HE].
[80] I. Tews, J. Margueron, and S. Reddy, Phys. Rev. C **98**, 045804 (2018), arXiv:1804.02783 [nucl-th].
[81] J. M. Lattimer and M. Prakash, Phys. Rept. **621**, 127 (2016), arXiv:1512.07820 [astro-ph.SR].
[82] C. C. Moustakidis, T. Gaitanos, C. Margaritis, and G. Lalazissis, Phys. Rev. C **95**, 045801 (2017), [Erratum: Phys.Rev.C 95, 059904 (2017)], arXiv:1608.00344 [nucl-th].
[83] C. Margaritis, P. Koliogiannis, and C. Moustakidis, Phys. Rev. D **101**, 043023 (2020), arXiv:1910.05767 [nucl-th].
[84] M. G. Alford and S. Han, Eur. Phys. J. A **52**, 62 (2016), arXiv:1508.01261 [nucl-th].
[85] K. Chatziioannou and S. Han, Phys. Rev. D **101**, 044019 (2020), arXiv:1911.07091 [gr-qc].
[86] S. Han and A. W. Steiner, Phys. Rev. D **99**, 083014 (2019), arXiv:1810.10967 [nucl-th].
[87] P. Haensel and J. Zdunik, Nature **340**, 617 (1989).
[88] J. M. Lattimer and M. Prakash, "What a Two Solar Mass Neutron Star Really Means," in *From Nuclei to Stars: Festschrift in Honor of Gerald E Brown*, edited by S. Lee (World Scientific, 2011) pp. 275–304, arXiv:1012.3208 [astro-ph.SR].
[89] S. Han and M. Prakash, Astrophys. J. **899**, 2 (2020), arXiv:2006.02207 [astro-ph.HE].
[90] K. Hebeler, J. Lattimer, C. Pethick, and A. Schwenk, Phys. Rev. Lett. **105**, 161102 (2010), arXiv:1007.1746 [nucl-th].
[91] A. Bauswein, O. Just, H.-T. Janka, and N. Stergioulas, Astrophys. J. Lett. **850**, L34 (2017), arXiv:1710.06843 [astro-ph.HE].
[92] A. L. Watts *et al.*, Rev. Mod. Phys. **88**, 021001 (2016), arXiv:1602.01081 [astro-ph.HE].
[93] L. McLerran and S. Reddy, Phys. Rev. Lett. **122**, 122701 (2019), arXiv:1811.12503 [nucl-th].
[94] E. D. Van Oeveren and J. L. Friedman, Phys. Rev. D **95**, 083014 (2017), arXiv:1701.03797 [gr-qc].
[95] E. Chabanat, P. Bonche, P. Haensel, J. Meyer, and R. Schaeffer, Nuclear Physics A **635**, 231 (1998).
[96] I. Tews, J. M. Lattimer, A. Ohnishi, and E. E. Kolomeitsev, Astrophys. J. **848**, 105 (2017), arXiv:1611.07133 [nucl-th].
[97] J. M. Lattimer and Y. Lim, Astrophys. J. **771**, 51 (2013), arXiv:1203.4286 [nucl-th].

[98] L. Lindblom, Phys. Rev. D **82**, 103011 (2010), arXiv:1009.0738 [astro-ph.HE].
[99] L. Lindblom and N. M. Indik, Phys. Rev. D **86**, 084003 (2012), arXiv:1207.3744 [astro-ph.HE].
[100] L. Lindblom and N. M. Indik, Phys. Rev. D **89**, 064003 (2014), [Erratum: Phys.Rev.D 93, 129903 (2016)], arXiv:1310.0803 [astro-ph.HE].
[101] J. S. Read, B. D. Lackey, B. J. Owen, and J. L. Friedman, Phys. Rev. D **79**, 124032 (2009), arXiv:0812.2163 [astro-ph].
[102] C. J. Horowitz and J. Piekarewicz, Phys. Rev. C **64**, 062802 (2001), arXiv:nucl-th/0108036.
[103] T. E. Riley *et al.*, Astrophys. J. Lett. **887**, L21 (2019), arXiv:1912.05702 [astro-ph.HE].
[104] M. Miller *et al.*, Astrophys. J. Lett. **887**, L24 (2019), arXiv:1912.05705 [astro-ph.HE].
[105] M. Ruiz, S. L. Shapiro, and A. Tsokaros, Phys. Rev. D **97**, 021501 (2018), arXiv:1711.00473 [astro-ph.HE].
[106] L. Rezzolla, E. R. Most, and L. R. Weih, Astrophys. J. Lett. **852**, L25 (2018), arXiv:1711.00314 [astro-ph.HE].
[107] B. P. Abbott *et al.* (LIGO Scientific, Virgo), Class. Quant. Grav. **37**, 045006 (2020), arXiv:1908.01012 [gr-qc].
[108] D. Radice, A. Perego, F. Zappa, and S. Bernuzzi, Astrophys. J. Lett. **852**, L29 (2018), arXiv:1711.03647 [astro-ph.HE].
[109] M. W. Coughlin *et al.*, Mon. Not. Roy. Astron. Soc. **480**, 3871 (2018), arXiv:1805.09371 [astro-ph.HE].
[110] K. Kiuchi, K. Kyutoku, M. Shibata, and K. Taniguchi, Astrophys. J. Lett. **876**, L31 (2019), arXiv:1903.01466 [astro-ph.HE].
[111] P. Landry, R. Essick, and K. Chatziioannou, Phys. Rev. D **101**, 123007 (2020), arXiv:2003.04880 [astro-ph.HE].
[112] R. Essick, I. Tews, P. Landry, S. Reddy, and D. E. Holz (2020) arXiv:2004.07744 [astro-ph.HE].
[113] J.-L. Jiang, S.-P. Tang, Y.-Z. Wang, Y.-Z. Fan, and D.-M. Wei, Astrophys. J. **892**, 1 (2020), arXiv:1912.07467 [astro-ph.HE].
[114] M. Al-Mamun, A. W. Steiner, J. Nttil, J. Lange, R. O'Shaugnessy, I. Tews, S. Gandolfi, C. Heinke, and S. Han (2020) arXiv:2008.12817 [astro-ph.HE].
[115] T. Zhao and J. M. Lattimer, in preparation (2020).
[116] D. Reardon *et al.*, Mon. Not. Roy. Astron. Soc. **455**, 1751 (2016), arXiv:1510.04434 [astro-ph.HE].
[117] P. Danielewicz, R. Lacey, and W. G. Lynch, Science **298**, 1592 (2002), arXiv:nucl-th/0208016.
[118] C. Constantinou, B. Muccioli, M. Prakash, and J. M. Lattimer, Phys. Rev. C **92**, 025801 (2015), arXiv:1504.03982 [astro-ph.SR].
[119] B. Abbott *et al.* (LIGO Scientific, Virgo), Astrophys. J. Lett. **892**, L3 (2020), arXiv:2001.01761 [astro-ph.HE].
[120] R. Abbott *et al.* (LIGO Scientific, Virgo), Astrophys. J. **896**, L44 (2020), arXiv:2006.12611 [astro-ph.HE].
[121] R. J. Foley, D. A. Coulter, C. D. Kilpatrick, A. L. Piro, E. Ramirez-Ruiz, and J. Schwab, Mon. Not. Roy. Astron. Soc. **494**, 190 (2020), arXiv:2002.00956 [astro-ph.HE].
[122] G. Baym and S. Chin, Phys. Lett. B **62**, 241 (1976).
[123] Y. Nambu and G. Jona-Lasinio, Phys. Rev. **122**, 345 (1961).
[124] A. Kurkela, P. Romatschke, and A. Vuorinen, Phys. Rev. D **81**, 105021 (2010), arXiv:0912.1856 [hep-ph].
[125] M. Alford, M. Braby, M. Paris, and S. Reddy, Astrophys. J. **629**, 969 (2005), arXiv:nucl-th/0411016.
[126] T. Kojo, P. D. Powell, Y. Song, and G. Baym, Phys. Rev. D **91**, 045003 (2015), arXiv:1412.1108 [hep-ph].
[127] T. Klähn and T. Fischer, Astrophys. J. **810**, 134 (2015), arXiv:1503.07442 [nucl-th].
[128] R. Gomes, P. Char, and S. Schramm, Astrophys. J. **877**, 139 (2019), arXiv:1806.04763 [nucl-th].
[129] S. Han, M. Mamun, S. Lalit, C. Constantinou, and M. Prakash, Phys. Rev. D **100**, 103022 (2019), arXiv:1906.04095 [astro-ph.HE].
[130] G. Baym, T. Hatsuda, T. Kojo, P. D. Powell, Y. Song, and T. Takatsuka, Rept. Prog. Phys. **81**, 056902 (2018), arXiv:1707.04966 [astro-ph.HE].
[131] E. Annala, T. Gorda, A. Kurkela, J. Nttil, and A. Vuorinen, Nature Phys. (2020), 10.1038/s41567-020-0914-9, arXiv:1903.09121 [astro-ph.HE].
[132] J. Hoppe, C. Drischler, K. Hebeler, A. Schwenk, and J. Simonis, Phys. Rev. C **100**, 024318 (2019), arXiv:1904.12611 [nucl-th].
[133] T. Hther, K. Vobig, K. Hebeler, R. Machleidt, and R. Roth, Phys. Lett. B **808**, 135651 (2020), arXiv:1911.04955 [nucl-th].
[134] S. Binder, J. Langhammer, A. Calci, and R. Roth, Phys. Lett. B **736**, 119 (2014), arXiv:1312.5685 [nucl-th].
[135] V. Lapoux, V. Som, C. Barbieri, H. Hergert, J. Holt, and S. Stroberg, Phys. Rev. Lett. **117**, 052501 (2016), arXiv:1605.07885 [nucl-ex].
[136] E. Epelbaum, H. Krebs, and P. Reinert, Front. in Phys. **8**, 98 (2020), arXiv:1911.11875 [nucl-th].
[137] A. Dyhdalo, R. Furnstahl, K. Hebeler, and I. Tews, Phys. Rev. C **94**, 034001 (2016), arXiv:1602.08038 [nucl-th].
[138] J. Hoppe, C. Drischler, R. Furnstahl, K. Hebeler, and A. Schwenk, Phys. Rev. C **96**, 054002 (2017), arXiv:1707.06438 [nucl-th].
[139] B. Carlsson, A. Ekstrm, C. Forssn, D. Strmberg, G. Jansen, O. Lilja, M. Lindby, B. Mattsson, and K. Wendt, Phys. Rev. X **6**, 011019 (2016), arXiv:1506.02466 [nucl-th].
[140] S. Wesolowski, N. Klco, R. Furnstahl, D. Phillips, and A. Thapaliya, J. Phys. G **43**, 074001 (2016), arXiv:1511.03618 [nucl-th].
[141] S. Wesolowski, R. Furnstahl, J. Melendez, and D. Phillips, J. Phys. G **46**, 045102 (2019), arXiv:1808.08211 [nucl-th].
[142] K. Huang, J. Hu, Y. Zhang, and H. Shen (2020) arXiv:2008.04491 [nucl-th].
[143] E. R. Most, L. J. Papenfort, L. R. Weih, and L. Rezzolla (2020) arXiv:2006.14601 [astro-ph.HE].
[144] N.-B. Zhang and B.-A. Li (2020) arXiv:2007.02513 [astro-ph.HE].
[145] V. Dexheimer, R. Gomes, T. Klähn, S. Han, and M. Salinas (2020) arXiv:2007.08493 [astro-ph.HE].
[146] A. Sedrakian, F. Weber, and J.-J. Li, Phys. Rev. D **102**, 041301 (2020), arXiv:2007.09683 [astro-ph.HE].
[147] J. Boguta, Phys. Lett. B **106**, 255 (1981).
[148] J. Lattimer, M. Prakash, C. Pethick, and P. Haensel, Phys. Rev. Lett. **66**, 2701 (1991).
[149] A. Cherman, T. D. Cohen, and A. Nellore, Phys. Rev. D **80**, 066003 (2009), arXiv:0905.0903 [hep-th].
[150] J. M. Maldacena, Int. J. Theor. Phys. **38**, 1113 (1999), arXiv:hep-th/9711200.
[151] C. Ecker, C. Hoyos, N. Jokela, D. Rodríguez Fernández, and A. Vuorinen, JHEP **11**, 031 (2017),

arXiv:1707.00521 [hep-th].
[152] T. Ishii, M. Järvinen, and G. Nijs, JHEP **07**, 003 (2019), arXiv:1903.06169 [hep-ph].
[153] P. M. Hohler and M. A. Stephanov, Phys. Rev. D **80**, 066002 (2009), arXiv:0905.0900 [hep-th].
[154] P. Romatschke and U. Romatschke, *Relativistic Fluid Dynamics In and Out of Equilibrium*, Cambridge Monographs on Mathematical Physics (Cambridge University Press, 2019) arXiv:1712.05815 [nucl-th].
[155] P. Bedaque and A. W. Steiner, Phys. Rev. Lett. **114**, 031103 (2015), arXiv:1408.5116 [nucl-th].
[156] I. Tews, J. Carlson, S. Gandolfi, and S. Reddy, Astrophys. J. **860**, 149 (2018), arXiv:1801.01923 [nucl-th].